Research Square

Preprints are preliminary reports that have not undergone peer review.
They should not be considered conclusive, used to inform clinical practice,
or referenced by the media as validated information.

High entropy diborides, closo-borates and hydrogen-carrying liquids as new radiation shields: A Geant4 study of photon, neutron and heavy ion attenuation

Mavia Anjum

mav.mavia14@gmail.com

University of Idaho

Ansar Abbas

COMSATS University Islamabad

Ali Zaman

COMSATS University Islamabad

Hannan Younis

COMSATS University Islamabad

Research Article

Keywords: Geant4, Radiation shielding, Mass attenuation coefficient, Neutron attenuation, Buildup factor, High entropy ceramics, Heavy ions, Dose equivalent

Posted Date: November 10th, 2026

DOI: https://doi.org/10.21203/rs.3.rs-11371913/v1

License: This work is licensed under a Creative Commons Attribution 4.0 International License.
Read Full License

Additional Declarations: No competing interests reported.

High entropy diborides, closo-borates and hydrogen-carrying liquids as new radiation shields: A Geant4 study of photon, neutron and heavy ion attenuation

Mavia Anjum[a *] Ansar Abbas[b], Ali Zaman[b], Hannan Younis[b]

[a] Department of Physics, University of Idaho, Moscow, Idaho 83844, USA

[b]Radiation Physics Lab, COMSATS University Islamabad, Islamabad, Pakistan

*Corresponding author. E-mail address: mav.mavia14@gmail.com (Mavia Anjum).

Abstract

Radiation shielding is required in nuclear facilities, accelerators, hospitals and spacecraft. Most studies on new shielding materials examine one type of radiation and use different codes and parameters, which makes comparison difficult. This study evaluated the photon, neutron and heavy ion shielding of 42 materials, including 26 candidates which were never studied for shielding, using a single validated Geant4 framework. Geant4 11.4.3 with the Shielding physics list was used. Mass attenuation coefficient, half value layer (HVL), tenth value layer (TVL), effective atomic number and buildup factors were calculated from 0.015 to 15 MeV. Neutron removal coefficients, secondary photons and spectra were calculated for thermal, fast and ^{252}Cf neutrons. Dose equivalent was calculated for protons, helium and iron ions. Simulated photon attenuation agreed with calculated values within 0.75% below 15 MeV, and fast neutron cross sections agreed within 0.5%. The QBBC physics list deviated by up to 99.6% for thermal neutrons in boron and gadolinium compounds. Neutron attenuation per unit mass was strongly correlated with hydrogen content ($r = 0.968$). The ^{10}B enriched $(TiZrHfNbTa)B_2$ high entropy diboride showed the shortest ^{252}Cf TVL of 12.7 cm, compared with 15.9 cm for polyethylene. Its HVL at 662 keV was 0.99 cm, and its removal coefficient for 14.1 MeV neutrons was 2.3 times that of polyethylene. Gadolinium bearing materials captured almost all thermal neutrons but emitted up to 2.1 photons per neutron. Behind 20 g/cm², LiH reduced the dose equivalent of 1 GeV/n iron ions to 0.49, compared with 0.63 for polyethylene and 0.90 for lead. In conclusion, the high entropy diboride is the most promising unexplored material for mixed field shielding. $Li_2B_{12}H_{12}$, liquid organic hydrogen carriers and deep eutectic solvents are promising light alternatives to polyethylene.

Keywords: Geant4, Radiation shielding, Mass attenuation coefficient, Neutron attenuation, Buildup factor, High entropy ceramics, Heavy ions, Dose equivalent

1. Introduction

Ionizing radiation is used and produced in nuclear power plants, fusion devices, particle accelerators, hospitals, industrial radiography and space missions [1,2]. Exposure to ionizing radiation can cause harmful effects to human health and can damage electronic devices and materials. Therefore, shielding is the primary method of protection wherever radiation is present [3]. The selection of a shielding material depends upon the type and energy of the radiation, the available space and weight, the secondary radiation produced inside the shield, and the mechanical, thermal and chemical stability of the material.

Lead, tungsten and concrete are the conventional shields for gamma rays. Polyethylene, often loaded with boron, is the conventional shield for neutrons and heavy ions [1,4,5]. However, each of these materials has limitations. Lead is toxic and mechanically weak and produces secondary neutrons under high energy hadrons. Concrete requires large thickness. Polyethylene has a low melting point and provides almost no attenuation for gamma rays. Hence, there is a continuous search for new materials which can attenuate more than one type of radiation, are lighter or more compact, and produce less secondary radiation.

Monte Carlo simulation codes are widely used to evaluate the shielding performance of new materials. Geant4 is an open source Monte Carlo toolkit that simulates the passage of particles through matter [6–8]. It combines electromagnetic, hadronic and high precision neutron physics in one framework and allows any material and geometry to be defined. Its accuracy has been benchmarked for medical physics applications [9], and its neutron transport package has been improved with modern evaluated nuclear data libraries [10,11].

Several studies have evaluated new shielding materials using XCOM [12], Phy-X/PSD [13] and Geant4 [14–16]. Other studies have evaluated hydrogen rich materials, metal hydrides and polymers for space radiation shielding [17–19]. However, most of these studies report only one type of radiation, use different codes, physics settings and sources, and rarely report the secondary photons produced by neutron capture. Furthermore, many families of modern materials contain hydrogen, boron, lithium, gadolinium and heavy elements, which are the key elements for shielding, but their radiation transport has not been studied. Therefore, a comprehensive comparison of conventional and new materials for photons, neutrons and heavy ions under the same conditions is lacking.

This study aims to address this gap. The objective of this study is to evaluate the photon, neutron and heavy ion shielding performance of 42 materials using a single validated Geant4 framework. The present study was designed to (i) validate the simulated photon and neutron attenuation against calculated and evaluated data, (ii) calculate μ/ρ, HVL, TVL, MFP, Z_{eff} and buildup factors for photons, (iii) calculate the

neutron removal coefficient, transmitted spectra, secondary photons, captures and albedo for five neutron sources, (iv) calculate the dose equivalent behind shields for protons, helium and iron ions, (v) quantify radiation streaming through triply periodic minimal surface (TPMS) lattices, and (vi) identify the relationship between composition and shielding parameters using Pearson's correlation. The findings of this study are essential for the selection of new shielding materials and for planning experimental studies on the most promising candidates.

2. Literature review

2.1. Geant4 in radiation shielding studies

Geant4 is a C++ toolkit in which geometry, materials, physics processes and scoring are defined separately [6,7]. The physics is selected through reference physics lists. The Shielding physics list was developed for shielding and underground applications and uses high precision, data driven neutron models below 20 MeV. General purpose lists such as QBBC use parametrised cross sections for low energy neutrons [20]. Later versions of Geant4 added improved electromagnetic models, parameterised geometries and multithreading [8]. The Neutron-HP package reads evaluated nuclear data [10] derived from libraries such as ENDF/B-VIII.0 [11]. The G4-Med collaboration has benchmarked the electromagnetic and hadronic physics of Geant4 against experimental data [9].

In gamma shielding studies, Geant4 has been used to calculate the attenuation of new glasses, steels and alloys, and the results were compared with XCOM [12,21] and with experiments [14,15]. Tunç et al. [16] combined Geant4 and EpiXS to study the effect of the Re/Nb ratio on gamma attenuation in high entropy alloys. Yilmaz Alan et al. [22] evaluated the gamma and neutron shielding of high entropy carbides. In space radiation studies, Geant4 and its MULASSIS interface have been used to calculate the dose behind regolith, polymer and hydride shields [17,18]. Luoni et al. [19] compared measured and simulated dose attenuation in innovative shielding materials. However, the choice of physics list for low energy neutrons is rarely justified in these studies, and validation is often reported for one type of radiation only.

2.2. Photon shielding parameters

The linear attenuation coefficient (μ), mass attenuation coefficient (μ/ρ), HVL, TVL and MFP describe the narrow beam attenuation of photons. Reference values of these parameters are tabulated by Hubbell and Seltzer [21] and calculated by XCOM [12]. The effective atomic number describes a compound in terms of an equivalent element and is routinely reported by Phy-X/PSD [13]. In broad beam geometry, scattered photons increase the transmitted fluence, and this increase is described by the buildup factor.

Most tabulated buildup factors are based on the geometric progression fitting method of Harima [23]. Direct Monte Carlo calculation of buildup factors for new materials is still uncommon.

2.3. Neutron shielding and secondary radiation

Fast neutrons are mainly slowed down by elastic scattering on hydrogen, and thermal neutrons are absorbed by nuclides with large capture cross sections such as ^{10}B, ^{6}Li and ^{157}Gd [11]. This explains the use of borated polyethylene and the interest in hydrides. Lithium and boron hydrides, metal organic frameworks (MOFs) and carbon composites have been proposed as hydrogen rich shields [4,18]. Li et al. [24] synthesised boron and lithium imidazolate frameworks for neutron shielding. Hu et al. [25] studied the thermal behaviour of a polymer and MOF based neutron shield. Chen et al. [26] reviewed gadolinium based composites for neutron and gamma shielding. Gadolinium has the largest thermal neutron capture cross section of all stable elements, but its capture is followed by a cascade of energetic gamma rays [26]. These secondary gamma rays are important in mixed neutron and gamma fields, but most studies on new materials report only neutron transmission.

2.4. High energy charged particles

For protons and heavy ions, the dose equivalent behind the shield depends on the energy loss of primary particles, nuclear fragmentation and secondary neutrons. The quality factor Q(L) defined in ICRP Publication 60 [27] and retained in ICRP Publication 103 [3] weights the absorbed dose by the linear energy transfer (LET) of particles. Guetersloh et al. [1] showed that polyethylene reduces the dose equivalent of heavy ions more effectively per unit mass than aluminum or lead. Slaba et al. [2] showed that the benefit of additional shielding thickness saturates for galactic cosmic rays and that hydrogen rich materials perform best. Naito et al. [5] and Luoni et al. [19] confirmed the advantage of hydrogen rich materials such as LiH. Stopping powers and ranges of protons and helium ions are tabulated in PSTAR and ASTAR [28] and SRIM [29].

2.5. Material families not yet evaluated for shielding

High entropy alloys were introduced in 2004 as alloys with multiple principal elements [30,31]. High entropy diborides such as $(Ti,Zr,Hf,Nb,Ta)B_2$ are ultrahigh temperature ceramics which contain heavy elements and about 15 wt% boron [32]. No shielding study on high entropy diborides was found, although high entropy carbides have been evaluated [22]. MAX phases are machinable and damage tolerant layered carbides and nitrides [33], and Ti based MAX phases have shown good tolerance to irradiation [34]. Their boride analogues, the MAB phases, have been reviewed by Kota et al. [35], and

MoAlB has shown radiation tolerance comparable to MAX phases [36]. However, attenuation data for MAX phases were not found.

Covalent organic frameworks such as COF-1 [37] contain about 16 wt% boron in a light porous solid. MOF-5 [38] is light and porous, radiation resistant MOFs have been reported [39], and lanthanide MOFs can carry gadolinium. Liquid organic hydrogen carriers (LOHCs) such as methylcyclohexane and perhydro dibenzyltoluene store hydrogen in a liquid and non flammable form [40]. Deep eutectic solvents (DES), first reported for choline chloride and urea [41], are inexpensive and non volatile and can dissolve salts [42]. Salt hydrates such as Glauber's salt and $CaCl_2 \cdot 6H_2O$ are used as phase change materials (PCMs) for thermal energy storage [43]. Clathrate hydrates of methane and tetrahydrofuran contain 11 to 13 wt% hydrogen [44]. Graphane, a fully hydrogenated graphene, was predicted by Sofo et al. [45] and produced by Elias et al. [46]. Ammonia borane [47] and $LiBH_4$ [48] are well known hydrogen storage materials, whereas the closo borate $Li_2B_{12}H_{12}$, which forms during the decomposition of $LiBH_4$ [49], has not been evaluated for shielding. Polyoxometalates such as $H_3PW_{12}O_{40}$ are tungsten oxide clusters that can be dispersed in polymers [50]. Melanin is of interest because melanised fungi grow under ionizing radiation [51]. TPMS lattices can now be produced by additive manufacturing [52], which raises the question whether two phase lattices can be used as graded shields.

2.6. Research gap

Three gaps were identified from the literature. Firstly, no photon, neutron or heavy ion transport data were found for most of the material families described in Section 2.5. Secondly, studies on new shields rarely report secondary photons, captures, albedo and transmitted spectra, although these quantities decide whether a neutron shield can be used in a mixed field. Thirdly, there is no common benchmark in which conventional, explored and new materials are compared under the same physics, sources and parameters for photons, neutrons and heavy ions. The present study addresses these three gaps.

3. Materials and methods

3.1. Selection of materials

Forty-two (n = 42) materials were studied and are listed in Table 1. The materials were divided into four groups. The reference group contained polyethylene, water, ordinary concrete, aluminum, lead, tungsten and borated polyethylene with 5 wt% boron. The explored group contained materials for which shielding studies already exist, namely LiH, ammonia borane, $LiBH_4$, $^6Li^{10}BH_4$, ZrH_2, B_4C, Gd_2O_3, MoAlB and the CoCrFeMnNi high entropy alloy. Tier 1 candidates were unexplored materials which are commercially

available or can be easily synthesised. Tier 2 candidates were unexplored materials whose synthesis or stability is less mature. Densities were taken from the literature where available (lit), otherwise nominal values were assigned (nom). The isotopically enriched materials ($^{6}Li^{10}BH_4$, COF-1 (^{10}B) and HEB (^{10}B)) were defined with 100% enrichment to show the upper limit of thermal neutron absorption. Elemental compositions were calculated from the chemical formulae, and NIST materials were used for the reference shields.

Table 1. Materials studied with their density (lit: literature value, nom: nominal value) and mass fractions of hydrogen, boron and gadolinium.

Material	Group	ρ (g/cm³)	H (wt%)	B (wt%)	Gd (wt%)
Polyethylene	Reference	0.94 (lit)	14.37	0	0
Water	Reference	1.00 (lit)	11.19	0	0
Ordinary concrete	Reference	2.30 (lit)	1.00	0	0
Aluminum	Reference	2.70 (lit)	0	0	0
Lead	Reference	11.35 (lit)	0	0	0
Tungsten	Reference	19.30 (lit)	0	0	0
Borated PE (5% B)	Reference	1.00 (nom)	13.65	5.0	0
LiH	Explored	0.78 (lit)	12.68	0	0
NH_3BH_3	Explored	0.78 (lit)	19.59	35.0	0
$LiBH_4$	Explored	0.666 (lit)	18.51	49.6	0
$^{6}Li^{10}BH_4$	Explored	0.613 (nom)	20.01	49.9	0
ZrH_2	Explored	5.61 (lit)	2.16	0	0
B_4C	Explored	2.52 (lit)	0	78.3	0
Gd_2O_3	Explored	7.41 (lit)	0	0	86.8
MoAlB	Explored	6.40 (nom)	0	8.1	0
CoCrFeMnNi	Explored	8.00 (nom)	0	0	0
COF-1	Tier 1	0.98 (nom)	3.11	16.7	0
COF-1 (^{10}B)	Tier 1	0.968 (nom)	3.14	15.7	0
LOHC (MCH)	Tier 1	0.77 (lit)	14.37	0	0
LOHC (H18-DBT)	Tier 1	0.91 (nom)	13.18	0	0
Glauber's salt	Tier 1	1.464 (lit)	6.26	0	0
$CaCl_2 \cdot 6H_2O$	Tier 1	1.71 (lit)	5.52	0	0
Epsomite	Tier 1	1.68 (lit)	5.73	0	0
Gypsum	Tier 1	2.32 (lit)	2.34	0	0
Reline (DES)	Tier 1	1.25 (lit)	8.54	0	0
Glyceline (DES)	Tier 1	1.19 (lit)	9.34	0	0
Reline + 5% $GdCl_3$	Tier 1	1.30 (nom)	8.11	0	3.0
CH_4 hydrate	Tier 1	0.91 (lit)	13.06	0	0
THF hydrate	Tier 1	0.98 (nom)	11.19	0	0
$(TiZrHfNbTa)B_2$	Tier 1	8.29 (nom)	0	15.5	0
HEB (^{10}B)	Tier 1	8.19 (nom)	0	14.5	0
Ti_3SiC_2	Tier 1	4.53 (lit)	0	0	0
Cr_2AlC	Tier 1	5.24 (lit)	0	0	0
Ti_2AlC	Tier 1	4.11 (lit)	0	0	0
MOF-5	Tier 2	0.59 (lit)	1.57	0	0
Gd-BDC MOF	Tier 2	1.90 (nom)	2.29	0	35.8
$Li_2B_{12}H_{12}$	Tier 2	1.30 (nom)	7.77	83.3	0
$H_3PW_{12}O_{40}$	Tier 2	2.85 (nom)	0.10	0	0

Material	Group	ρ (g/cm³)	H (wt%)	B (wt%)	Gd (wt%)
POSS (isobutyl)	Tier 2	1.13 (nom)	8.31	0	0
Gd-POSS (10% Gd)	Tier 2	1.25 (nom)	7.48	0	10.0
Graphane	Tier 2	1.50 (nom)	7.74	0	0
Melanin	Tier 2	1.40 (nom)	3.43	0	0

3.2. Geant4 simulation setup

All simulations were performed using Geant4 version 11.4.3 [8] in multithreaded mode on the Lemhi high performance computing cluster of the University of Idaho. The Shielding physics list with the option 4 electromagnetic constructor (Shielding_EMZ) was used, which uses high precision neutron models and evaluated data below 20 MeV [20]. All neutron and ion simulations were repeated with the QBBC physics list to quantify the dependence on physics models. The production cut was set to 0.1 mm.

The geometry consisted of a slab shield placed in vacuum, with scoring surfaces at its front and rear faces. The lateral size of the slab was set to at least twice ten mean free paths so that lateral leakage did not affect the broad beam results. For charged particles, a 1 cm thick water phantom was placed directly behind the shield, and the absorbed dose and dose equivalent were scored in it. Calculated reference values were obtained in the same program using G4EmCalculator for photons and charged particles and the Geant4 hadronic process store for neutrons. These values use the same data libraries as the transport, therefore their comparison with the simulated values tests the transport, geometry and scoring.

3.3. Radiation sources

Mono energetic photons at 16 energies from 0.015 to 15 MeV were used, including 0.0595, 0.662, 1.173, 1.25 and 1.332 MeV, which correspond to the gamma lines of ^{241}Am, ^{137}Cs and ^{60}Co. Five neutron sources were used, namely thermal neutrons (0.0253 eV), mono energetic neutrons of 1, 4.5 and 14.1 MeV, and a ^{252}Cf spontaneous fission spectrum following the Watt representation of ISO 8529-1 [53]. Neutron slabs were 1, 2, 5, 10, 15, 20 and 30 cm thick. Four charged particle beams were used, namely 100 MeV and 1 GeV protons, 1 GeV/n ^{4}He and 1 GeV/n ^{56}Fe ions, with shield areal densities of 1, 2, 5, 10, 20 and 30 g/cm².

3.4. Linear and mass attenuation coefficients

For photons, a pencil beam was used and a photon was counted as uncollided only if it reached the rear face without any interaction. The uncollided transmission (T) through a slab of thickness x is given by the Beer-Lambert law [21]:

$$T(x) = \frac{N(x)}{N_0} = e^{-\mu x} \qquad (1)$$

Here N_0 and N(x) are the number of incident and uncollided transmitted photons, respectively. The linear attenuation coefficient μ (cm^{-1}) was obtained by a weighted least squares fit of −ln T against x through the origin at 0.5, 1, 2 and 3 mean free paths. The mass attenuation coefficient (cm^2/g) was calculated as:

$$\mu_m = \frac{\mu}{\rho} \qquad (2)$$

where ρ is the density of the material in g/cm^3.

3.5. Half value layer, tenth value layer and mean free path

The thickness of a material which reduces the photon intensity to half and to one tenth of its initial value is called HVL and TVL, respectively. The MFP is the average distance travelled by a photon between two interactions [13]. These parameters were calculated as:

$$\mathrm{HVL} = \frac{\ln 2}{\mu} \qquad (3)$$

$$\mathrm{TVL} = \frac{\ln 10}{\mu} \qquad (4)$$

$$\mathrm{MFP} = \frac{1}{\mu} \qquad (5)$$

3.6. Effective atomic number

The effective atomic number was calculated using the direct method from the total atomic cross section (σ_a) and the total electronic cross section (σ_e) [13]:

$$Z_{\mathrm{eff}} = \frac{\sigma_a}{\sigma_e} \qquad (6)$$

$$\sigma_a = \frac{\mu/\rho}{N_A \sum_i w_i / A_i} \qquad (7)$$

$$\sigma_e = \frac{1}{N_A} \sum_i \frac{f_i A_i}{Z_i} \left(\frac{\mu}{\rho}\right)_i \qquad (8)$$

Here N_A is Avogadro's number, and w_i, f_i, A_i and Z_i are the mass fraction, number fraction, atomic weight and atomic number of element i, respectively.

3.7. Buildup factor

Buildup factors were calculated directly from the simulation for slab thicknesses of 0.5, 1, 2, 3, 4, 5, 7 and 10 mean free paths. The number buildup factor (B_N) is the ratio of the total to the uncollided transmitted photon number. The energy fluence buildup factor (B_E) is the ratio of the total to the uncollided transmitted energy fluence:

$$B_E = \frac{\sum_{\text{all}} E\ /\cos\theta}{\sum_{\text{uncollided}} E_0} \qquad (9)$$

Here E and θ are the energy and the angle to the slab normal of each photon leaving the rear face, and E_0 is the incident photon energy.

3.8. Neutron removal coefficient

At the rear face, transmitted neutrons were scored in three groups, namely thermal (below 0.5 eV), epithermal (0.5 eV to 0.1 MeV) and fast (above 0.1 MeV), together with their mean energy, transmitted photons, reflected neutrons (albedo) and radiative captures inside the slab. For mono energetic sources, the uncollided macroscopic total cross section (Σ_{tot}) was obtained in the same way as μ for photons. The effective removal coefficient (Σ_{eff}) was obtained from the slope of the logarithm of the total number of transmitted neutrons (N_n) against thickness:

$$\Sigma_{\text{eff}} = -\frac{\text{d}\ln N_n(x)}{\text{d}x} \qquad (10)$$

$$\text{TVL}_n = \frac{\ln 10}{\Sigma_{\text{eff}}} \qquad (11)$$

Σ_{eff} includes the scattered neutrons which leave the rear face and is therefore a practical broad beam parameter. It was also expressed per unit mass as Σ_{eff}/ρ. For comparison, the empirical fast neutron removal cross section (Σ_R) was calculated from the elemental mass removal cross sections and the composition of each material.

3.9. Dose equivalent and quality factor

The dose equivalent (H) in the water phantom was calculated event by event as the sum of energy deposits weighted by the quality factor Q(L) of ICRP Publication 60 [27]:

$$Q(L) = \begin{cases} 1, & L < 10\ \text{keV/μm} \\ 0.32L - 2.2, & 10 \le L \le 100\ \text{keV/μm} \\ 300/\sqrt{L}, & L > 100\ \text{keV/μm} \end{cases} \qquad (12)$$

Here L is the unrestricted LET in water. The results are reported as H/H_0, the ratio of the dose equivalent behind the shield to the unshielded dose equivalent. The mean quality factor was calculated as:

$$\bar{Q} = \frac{H}{D} \qquad (13)$$

where D is the absorbed dose in the phantom. Proton ranges and stopping powers were compared with PSTAR [28].

3.10. Triply periodic minimal surface lattices

Two phase lattices were built from the gyroid and Schwarz-P surfaces in a 5 cm slab using a voxelised parameterisation. Each voxel was assigned to phase A or phase B according to the sign of the level set function. Four lattices were simulated, namely a W and polyethylene gyroid with a 50% volume fraction, the same pair with a volume fraction graded through the thickness, a Gd_2O_3 and Glauber's salt gyroid with 25% Gd_2O_3, and a B_4C and LOHC Schwarz-P lattice with 48% B_4C. Each lattice was compared with a homogeneous slab of the same thickness and composition using 0.0595, 0.662 and 1.25 MeV photons, 4.5 MeV neutrons and ^{252}Cf neutrons.

3.11. Pearson's correlation coefficient

The relationship between composition and shielding parameters was evaluated using Pearson's correlation coefficient (r):

$$r = \frac{\sum_i (x_i - \bar{x})\,(y_i - \bar{y})}{\sqrt{\sum_i (x_i - \bar{x})^2 \sum_i (y_i - \bar{y})^2}} \qquad (14)$$

Here x_i and y_i are the values of two variables for material i, and $\bar{x}$ and $\bar{y}$ are their mean values. For n = 42, values of |r| above 0.30 and 0.39 are significant at $p < 0.05$ and $p < 0.01$, respectively.

3.12. Quality assurance and statistics

Photon simulations used 10^6 primaries per thickness, neutron simulations used 10^5 primaries per thickness and source, and ion simulations used 10^4 (iron) to 10^5 (100 MeV protons) primaries per areal density. TPMS simulations used 5×10^5 photons and 10^5 neutrons per case. The statistical uncertainty of the fitted photon coefficients was 0.07%, and the median uncertainty of the fitted neutron cross sections was 0.2%.

The median relative uncertainty of the dose equivalent was 1.8%, and it was larger only behind thick shields where the dose was very small. For quality assurance, the simulated μ and Σ_{tot} were compared with the calculated values, and the percentage deviation was calculated. Polyethylene was used as the reference material for all ratios.

4. Results and discussion

4.1. Validation of the simulation

The deviation of the simulated μ from the calculated values for all 42 materials at 16 energies is shown in Fig. 1(a), and selected values are compared in Table 2. All 630 values below 15 MeV agreed within 0.75%, with a mean absolute deviation of 0.07%. At 15 MeV, the simulated μ was higher than the calculated value by up to 2.9% (ZrH_2), and the largest deviations were observed for materials containing Zr, Gd, Hf, Ta, W, Pb or Mo. This is due to photonuclear absorption near the giant dipole resonance, which is included in the transport but not in the electromagnetic coefficients. The calculated μ/ρ of polyethylene at 1 MeV (0.0725 cm^2/g) agrees with the tabulated value [21]. Therefore, the photon results are reliable within the 1% level commonly accepted in shielding studies [13].

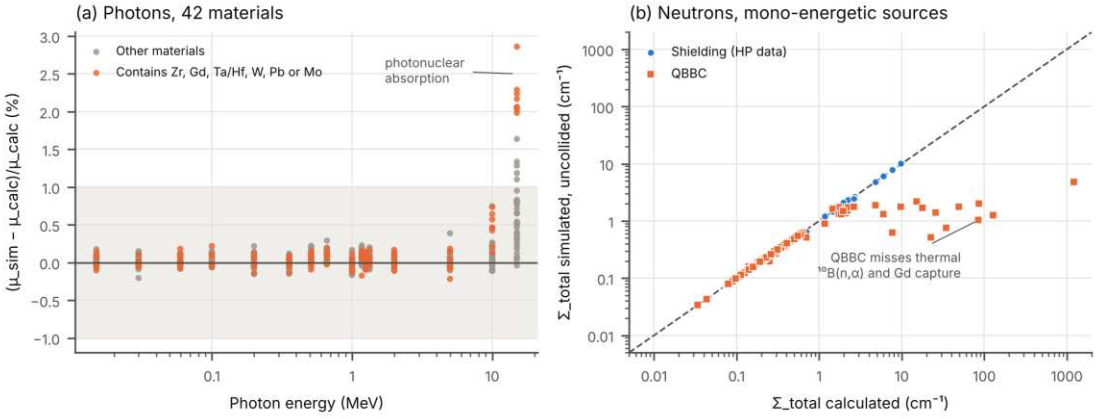


Fig. 1. Validation of the simulation. (a) Percentage deviation of the simulated linear attenuation coefficient from the calculated value for 42 materials. (b) Simulated against calculated uncollided neutron total cross sections for thermal, 1, 4.5 and 14.1 MeV neutrons using the Shielding and QBBC physics lists.

Table 2. Comparison of simulated (Sim.) and calculated (Calc.) mass attenuation coefficients (cm^2/g) for selected materials.

Material	μ/ρ 59.5 keV Sim.	μ/ρ 59.5 keV Calc.	Dev. (%)	μ/ρ 662 keV Sim.	μ/ρ 662 keV Calc.	Dev. (%)	μ/ρ 1.25 MeV Sim.	μ/ρ 1.25 MeV Calc.	Dev. (%)
Polyethylene	0.1973	0.1971	0.11	0.0880	0.0879	0.12	0.0648	0.0648	−0.06
Water	0.2061	0.2061	−0.02	0.0856	0.0856	0.03	0.0631	0.0631	−0.01
Concrete	0.2818	0.2819	−0.04	0.0777	0.0777	0.11	0.0572	0.0572	−0.02
Lead	5.0932	5.0871	0.12	0.1097	0.1097	0.06	0.0585	0.0585	−0.04
Tungsten	3.7223	3.7237	−0.04	0.0974	0.0975	−0.03	0.0557	0.0556	0.11
HEB (^{10}B)	2.9527	2.9525	0.01	0.0853	0.0852	0.14	0.0542	0.0542	−0.10
$Li_2B_{12}H_{12}$	0.1701	0.1701	0.01	0.0772	0.0771	0.04	0.0569	0.0569	−0.01

The comparison for neutrons is shown in Fig. 1(b). Using the Shielding physics list, the uncollided total cross sections agreed with the evaluated values within 0.5% at 1, 4.5 and 14.1 MeV, with a mean deviation of 0.16% (n = 126). For thermal neutrons, the mean deviation was 3.2% and the maximum was 9.6% (graphane). The thermal deviations were highest for hydrogen rich materials and are attributed to the treatment of thermal scattering by bound hydrogen. For strong thermal absorbers such as Gd_2O_3 and the ^{10}B compounds, no uncollided thermal neutrons were transmitted through 1 cm, so their thermal cross sections could not be extracted. Using the QBBC physics list, the deviations were up to 14% at 1 MeV and up to 99.6% for thermal neutrons in Gd_2O_3, Gd-BDC, B_4C, COF-1 (^{10}B), MoAlB and $^6Li^{10}BH_4$, with a mean of 44.6% at thermal energy. This shows that QBBC does not reproduce thermal neutron capture by ^{10}B and Gd. Therefore, data driven neutron physics must be used for neutron shielding below 20 MeV [10,20], and all neutron results in this study were obtained using the Shielding physics list. The proton CSDA ranges in water also agreed with PSTAR at 1, 10, 100 and 1000 MeV (Fig. S5) [28].

4.2. Photon attenuation

4.2.1. Mass attenuation coefficient and half value layer

The μ/ρ and HVL of selected materials are shown in Fig. 2, and the HVL and Z_{eff} values at three important energies are given in Table 3. At 15 keV, the μ/ρ of high Z materials was more than two orders of magnitude higher than that of light materials. Between 0.5 and 3 MeV, where Compton scattering is dominant, the μ/ρ of all materials converged within about 20%. Above about 5 MeV, pair production again favoured the high Z materials.

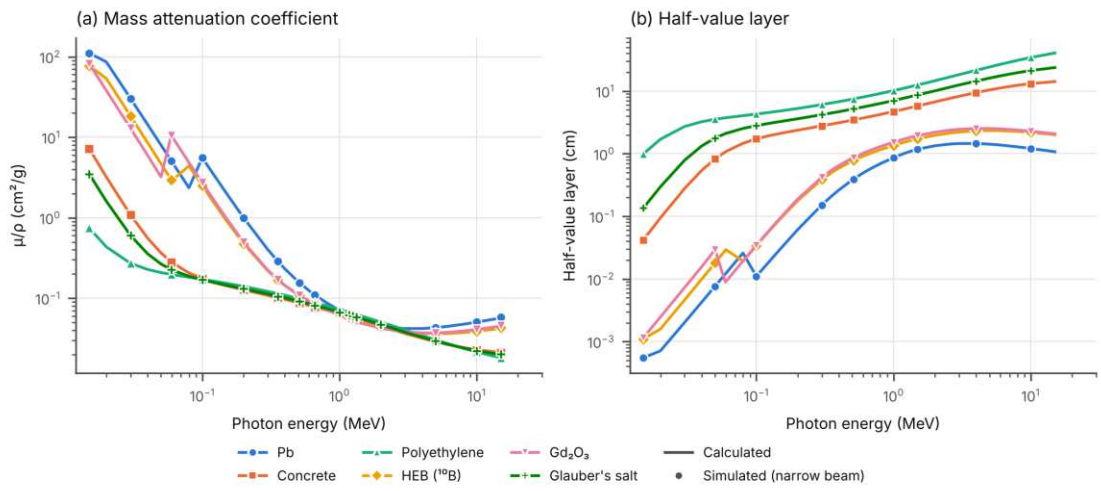


Fig. 2. (a) Mass attenuation coefficient and (b) half value layer of selected materials against photon energy. Lines show calculated values and markers show simulated values.

Table 3. Simulated half value layers at the ^{241}Am, ^{137}Cs and mean ^{60}Co energies and effective atomic number at 662 keV.

Material	ρ (g/cm³)	HVL 59.5 keV (cm)	HVL 662 keV (cm)	HVL 1.25 MeV (cm)	Z_{eff} at 662 keV
Polyethylene	0.94	3.737	8.382	11.378	2.7
Water	1.00	3.364	8.097	10.979	3.3
Concrete	2.30	1.069	3.876	5.266	8.6
Lead	11.35	0.012	0.557	1.044	82.0
Tungsten	19.30	0.010	0.369	0.645	74.0
Gd_2O_3	7.41	0.009	1.113	1.762	34.6
ZrH_2	5.61	0.033	1.653	2.341	14.7
MoAlB	6.40	0.034	1.469	2.071	20.7
CoCrFeMnNi	8.00	0.071	1.186	1.629	26.0
$(TiZrHfNbTa)B_2$	8.29	0.029	0.991	1.557	23.5
HEB (^{10}B)	8.19	0.029	0.992	1.563	23.5
Ti_3SiC_2	4.53	0.242	2.091	2.851	15.4
$H_3PW_{12}O_{40}$	2.85	0.084	2.617	4.351	27.6
$Li_2B_{12}H_{12}$	1.30	3.134	6.909	9.366	3.0
LiH	0.78	5.323	11.450	15.523	2.0
Reline + 5% $GdCl_3$	1.30	0.906	6.415	8.760	3.9
COF-1 (^{10}B)	0.968	3.910	9.022	12.215	4.7
LOHC (MCH)	0.77	4.567	10.237	13.877	2.7
MOF-5	0.59	1.614	15.285	20.838	7.2

The HVL of the high entropy diboride at 662 keV was found to be 0.99 cm, which is 1.8 times that of lead and 3.9 times smaller than that of concrete. Its Z_{eff} of 23.5 is due to the presence of Hf (Z = 72) and Ta (Z = 73) along with light B, Ti and Nb. The polyoxometalate $H_3PW_{12}O_{40}$ has a density of only 2.85 g/cm³ but a Z_{eff} of 27.6 due to its 77 wt% tungsten. Its HVL at 59.5 keV (0.084 cm) was about one third that of Ti_3SiC_2, although its density is 63% of that of Ti_3SiC_2. Therefore, these two candidates are the most effective new photon absorbers in this study. The addition of 3 wt% gadolinium to reline reduced its

HVL at 59.5 keV from 2.42 to 0.91 cm. This is due to the K absorption edge of gadolinium at 50.2 keV, which has also been reported for gadolinium composites [26].

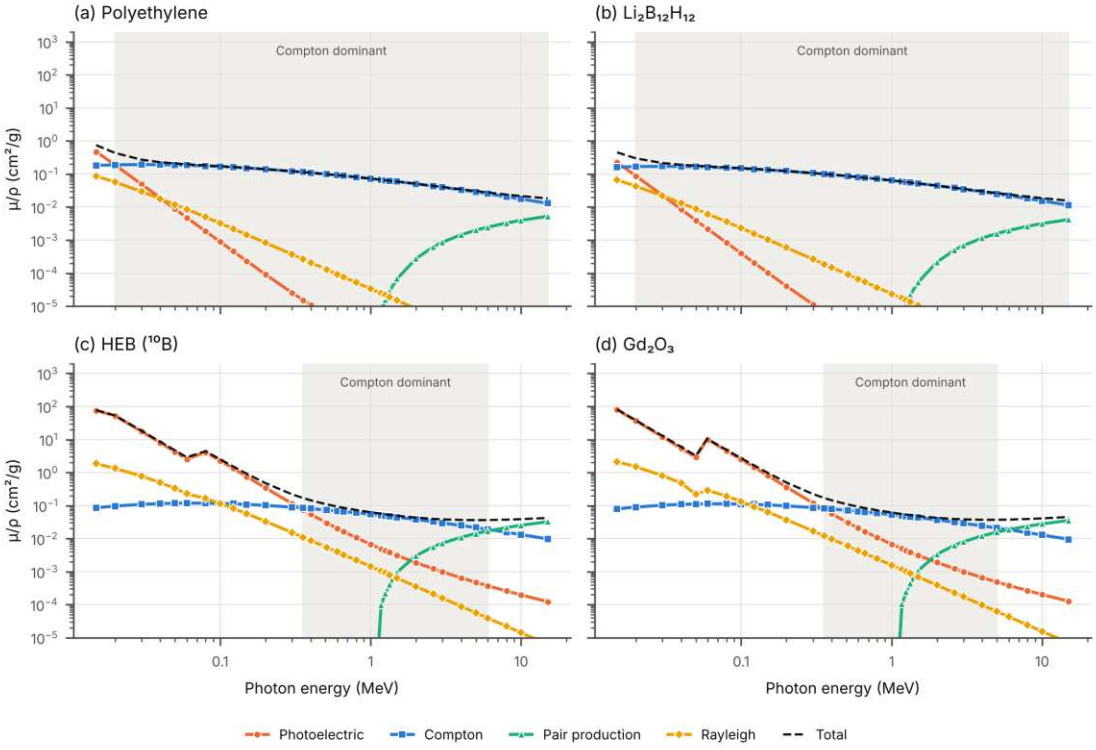


Fig. 3. Partial mass attenuation coefficients for photoelectric absorption, Compton scattering, pair production and Rayleigh scattering in (a) polyethylene, (b) $Li_2B_{12}H_{12}$, (c) HEB (^{10}B) and (d) Gd_2O_3. The shaded band shows the energy range where Compton scattering is dominant.

The partial interaction coefficients are shown in Fig. 3. In polyethylene and $Li_2B_{12}H_{12}$, Compton scattering was dominant from about 20 keV to above 15 MeV. In HEB and Gd_2O_3, the Compton dominant range was reduced to about 0.35 to 5 MeV. Below this range, photoelectric absorption with K edges at 50 keV (Gd) and 65 to 67 keV (Hf and Ta) increased the attenuation by orders of magnitude, and above this range pair production became dominant.

4.2.2. Effective atomic number

The Z_{eff} of six materials against photon energy is shown in Fig. 4. Z_{eff} varied strongly with energy for compounds that contain both heavy and light elements. For example, the Z_{eff} of the high entropy diboride decreased from 63 at 15 keV to 21 at 1.3 MeV. On the other hand, Z_{eff} was nearly constant above 0.1 MeV for concrete and Glauber's salt. Therefore, a single value of Z_{eff} is not sufficient to describe compositionally complex materials, and energy dependent values should be reported [13].

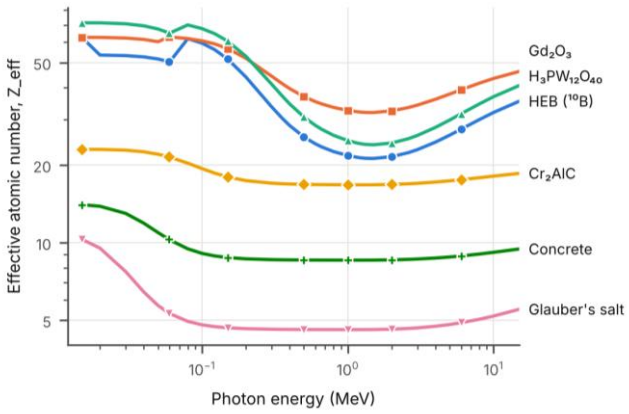


Fig. 4. Effective atomic number calculated by the direct method against photon energy for six materials.

4.2.3. Buildup factor

The B_E values at 5 and 10 mean free paths are shown in Fig. 5. For light materials, B_E was highest between 0.06 and 0.1 MeV, where multiple Compton scattering is not yet stopped by photoelectric absorption. At 10 mean free paths, B_E reached 82 for $Li_2B_{12}H_{12}$ and 65 for polyethylene. For the high entropy diboride, B_E did not exceed 6.8, and for lead and Gd_2O_3 it exceeded 7 at only two of the 16 energies, because the scattered photons are quickly absorbed. Two sharp peaks were observed for Gd_2O_3 at 59.5 keV and for lead at 100 keV. In both cases, the incident energy is just above the K edge, and the K fluorescence photons (about 43 keV for Gd and 75 keV for Pb) have a much longer mean free path than the primary photons. The geometric progression fitting method [23] smooths these features. Therefore, direct simulation gives a more realistic description of buildup for new high Z compounds near absorption edges.

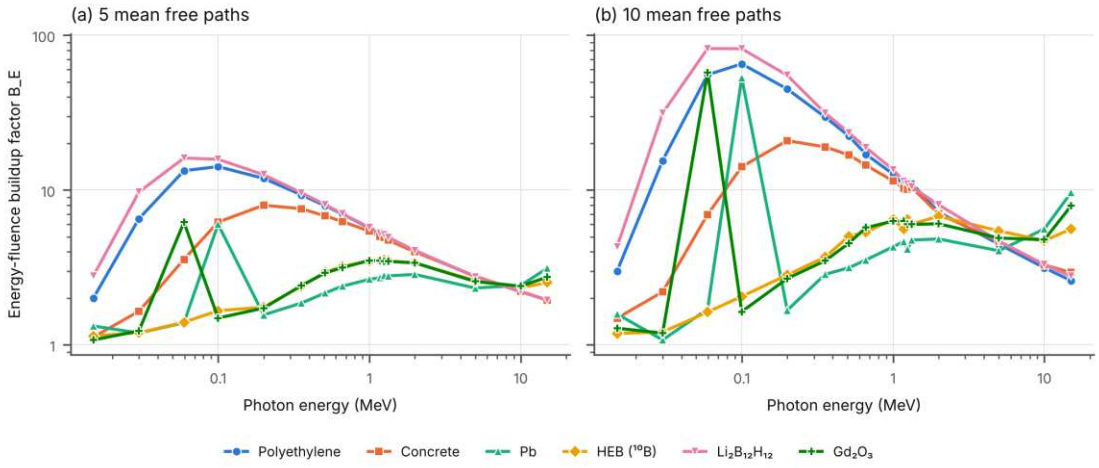


Fig. 5. Energy fluence buildup factor against photon energy at (a) 5 and (b) 10 mean free paths.

4.2.4. Mass efficiency of photon shields

The HVL at 662 keV is plotted against density in Fig. 6. All 42 materials lie close to the lines of constant areal density per HVL, between 6.3 g/cm² (lead) and 9.0 g/cm² (MOF-5). The results revealed that at 662 keV the mass required for a given attenuation is almost independent of composition. This is because Compton scattering is dominant at this energy and the number of electrons per gram is nearly the same for all materials. Hence, high Z materials save volume but not mass, and light hydrogenous materials are not penalised in mass for 662 keV photons but only in thickness.

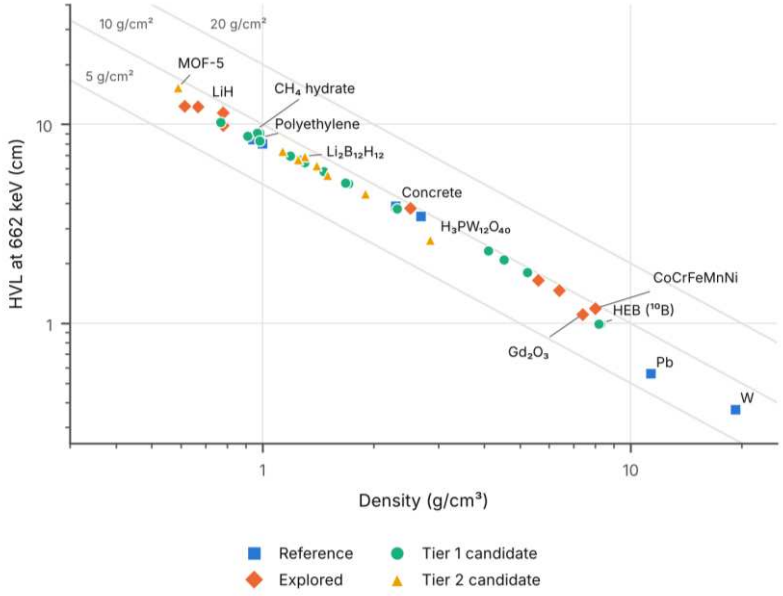


Fig. 6. Half value layer at 662 keV against density. Grey lines show constant areal density per HVL of 5, 10 and 20 g/cm².

4.3. Neutron attenuation

4.3.1. Neutron removal coefficient

The ^{252}Cf effective removal coefficients of all materials are shown in Fig. 7, and selected values are given in Table 4. Per unit thickness, the best materials were HEB (^{10}B) (0.182 cm^{-1}), $Li_2B_{12}H_{12}$ (0.179 cm^{-1}), ZrH_2 (0.176 cm^{-1}), ammonia borane (0.174 cm^{-1}) and borated polyethylene (0.171 cm^{-1}), compared with 0.145 cm^{-1} for polyethylene and 0.056 cm^{-1} for concrete. The corresponding TVLs were 12.7, 12.9, 13.1, 13.2 and 13.5 cm, compared with 15.9 cm for polyethylene, 41.3 cm for concrete and 55.0 cm for lead. Reline, Gd loaded reline and graphane were found to be equal to or better than polyethylene per unit thickness.

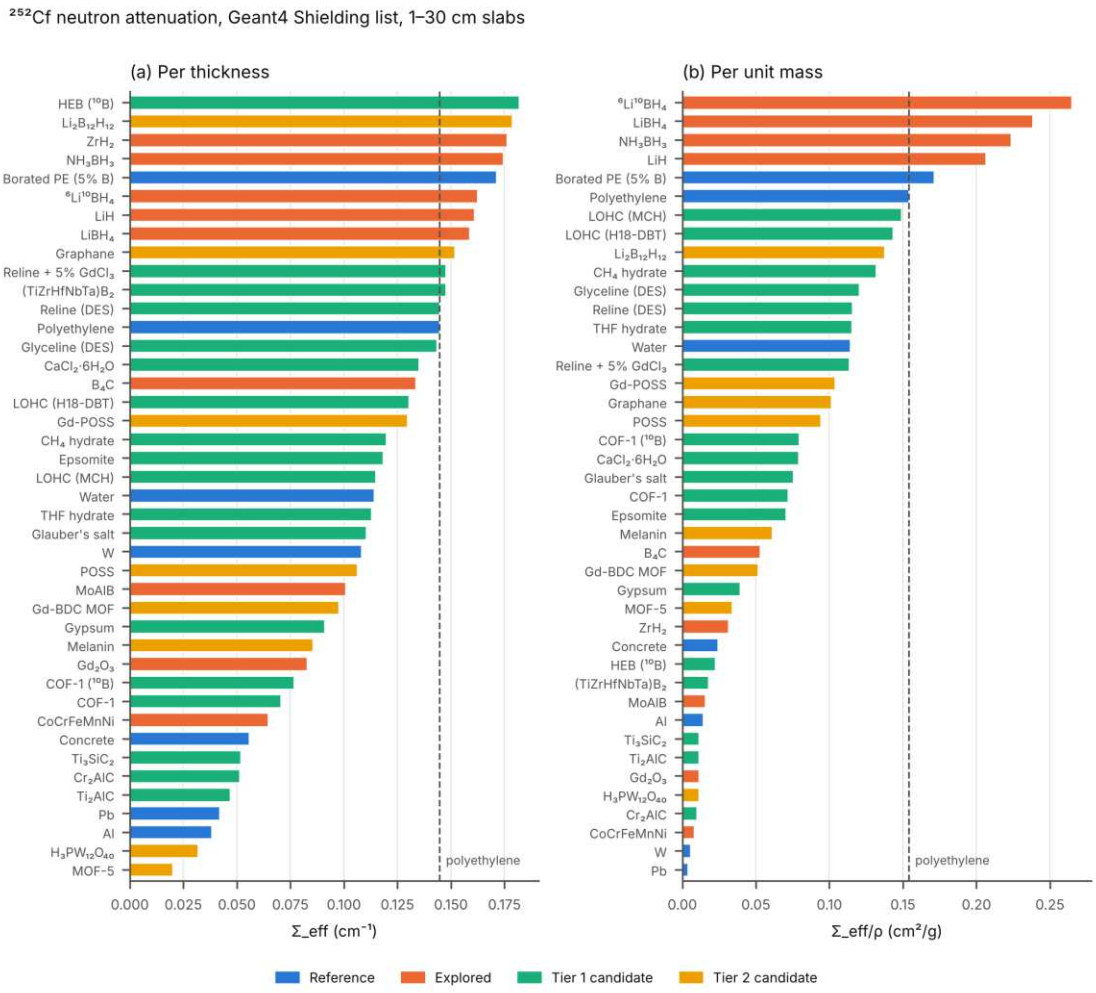


Fig. 7. Effective ^{252}Cf neutron removal coefficient of all materials (a) per unit thickness and (b) per unit mass. The dashed line shows polyethylene.

Table 4. Neutron shielding parameters of selected materials using the Shielding physics list. Photons out are the photons leaving the rear face of a 10 cm slab per incident ^{252}Cf neutron.

Material	Group	Σ_{eff} ^{252}Cf (cm^{-1})	Σ_{eff}/ρ ^{252}Cf (cm^2/g)	TVL ^{252}Cf (cm)	Photons out, 10 cm (per n)	Σ_{eff} 14.1 MeV (cm^{-1})
HEB (^{10}B)	Tier 1	0.182	0.022	12.7	0.038	0.113
$Li_2B_{12}H_{12}$	Tier 2	0.179	0.137	12.9	0.253	0.072
ZrH_2	Explored	0.176	0.031	13.1	0.123	0.079
NH_3BH_3	Explored	0.174	0.224	13.2	0.280	0.058
Borated PE (5% B)	Reference	0.171	0.171	13.5	0.249	0.058
$^6Li^{10}BH_4$	Explored	0.162	0.265	14.2	0.233	0.052
LiH	Explored	0.161	0.206	14.3	0.046	0.052
Graphane	Tier 2	0.152	0.101	15.2	0.132	0.062
$(TiZrHfNbTa)B_2$	Tier 1	0.148	0.018	15.6	0.046	0.096
Reline + 5% $GdCl_3$	Tier 1	0.148	0.114	15.6	0.744	0.055

Material	Group	Σ_{eff} ^{252}Cf (cm^{-1})	Σ_{eff}/ρ ^{252}Cf (cm^2/g)	TVL ^{252}Cf (cm)	Photons out, 10 cm (per n)	Σ_{eff} 14.1 MeV (cm^{-1})
Polyethylene	Reference	0.145	0.154	15.9	0.151	0.049
Reline (DES)	Tier 1	0.145	0.116	15.9	0.364	0.054
LOHC (H18-DBT)	Tier 1	0.130	0.143	17.7	0.125	0.044
CH_4 hydrate	Tier 1	0.120	0.132	19.2	0.115	0.042
Water	Reference	0.114	0.114	20.2	0.106	0.043
LOHC (MCH)	Tier 1	0.115	0.149	20.1	0.105	0.036
Concrete	Reference	0.056	0.024	41.3	0.034	0.043
Lead	Reference	0.042	0.004	55.0	0.017	0.015
MOF-5	Tier 2	0.020	0.034	115.2	0.017	0.010

Per unit mass, the order changed completely. The lithium and boron hydrides were the best, with $^{6}Li^{10}BH_4$ at 0.265 cm^2/g (1.7 times polyethylene), $LiBH_4$ at 0.238 cm^2/g and ammonia borane at 0.224 cm^2/g, while the dense ceramics and metals had the lowest values. The two LOHCs reached 0.93 to 0.97 of the polyethylene value per gram, which makes them the best unexplored hydrogenous liquids.

4.3.2. Effect of composition

The ^{252}Cf removal coefficient per unit mass is plotted against hydrogen and boron content in Fig. 8. Σ_{eff}/ρ followed the hydrogen content closely ($r = 0.968$, $n = 42$), whereas its correlation with boron content was weak ($r = 0.369$). This confirms that the attenuation of fast neutrons is controlled by moderation on hydrogen [2,4]. Boron and gadolinium improve the shielding mainly by absorbing the moderated neutrons which would otherwise diffuse out of the slab. This explains why B_4C, which has 78 wt% boron but no hydrogen, reached only 0.053 cm^2/g. Furthermore, the empirical removal cross section Σ_R was weakly correlated with the simulated fast removal coefficient ($r = 0.507$). Therefore, Σ_R values, which are widely used to rank new materials, should not replace transport calculations for compounds that contain hydrogen, boron and heavy elements together.

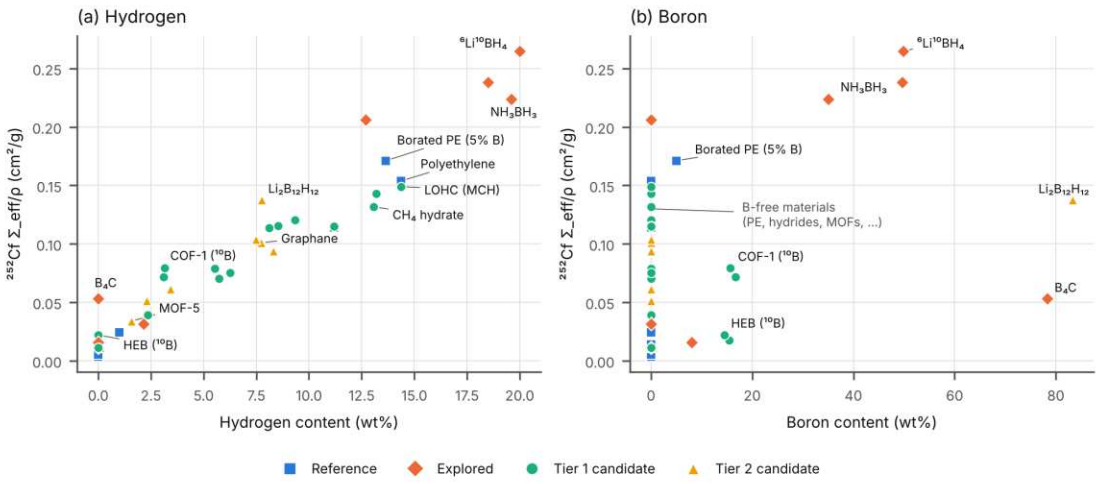


Fig. 8. ^{252}Cf effective removal coefficient per unit mass against (a) hydrogen and (b) boron mass fraction.

4.3.3. Effect of neutron energy

The dependence on source energy is shown in Fig. 9. For thermal neutrons, the uncollided cross sections of borated polyethylene (4.8 cm^{-1}) and Gd loaded reline (10.1 cm^{-1}) were 1.8 and 3.8 times that of polyethylene (2.6 cm^{-1}), and the strongest absorbers transmitted no uncollided thermal neutrons through 1 cm. At 1 MeV, polyethylene had the highest fast removal coefficient (0.39 cm^{-1}) due to the large elastic scattering cross section of hydrogen. As the energy increased to 14.1 MeV, the advantage of hydrogen decreased and inelastic scattering on heavy nuclei became important. At 14.1 MeV, the removal coefficient of HEB (^{10}B) was 0.113 cm^{-1}, which is 2.3 times that of polyethylene (0.049 cm^{-1}), and the natural diboride, B_4C and ZrH_2 reached 0.079 to 0.096 cm^{-1}. Hence, for D-T fusion neutrons, a dense boride is more effective per unit thickness than any hydrogenous material.

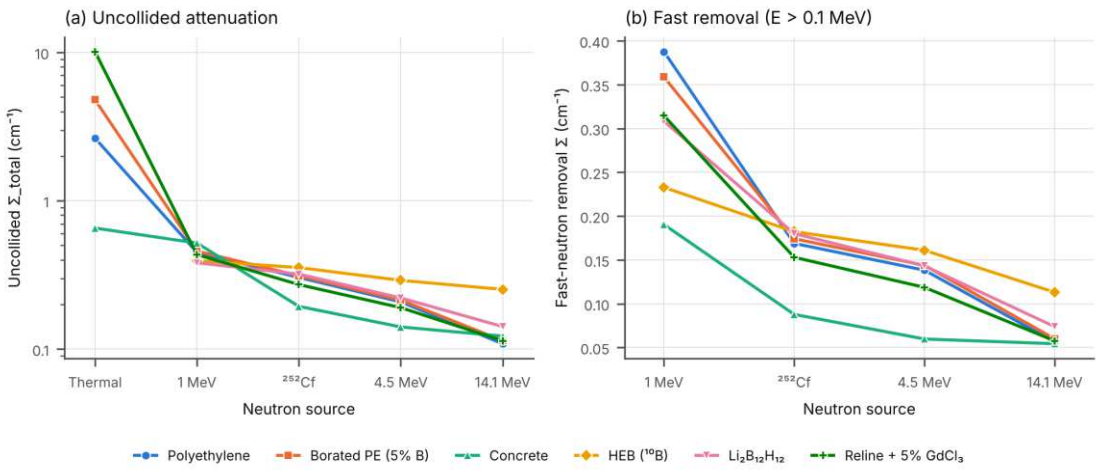


Fig. 9. Neutron attenuation against source energy. (a) Uncollided total cross section and (b) fast removal coefficient for neutrons above 0.1 MeV.

4.3.4. Secondary photons, captures and albedo

The photons leaving the rear face per incident neutron are shown in Fig. 10. For thermal neutrons, the gadolinium materials emitted the highest number of photons, with 2.09 photons per neutron behind 1 cm of Gd loaded reline, 2.00 for Gd-POSS, 1.71 for Gd-BDC MOF and 1.03 for Gd_2O_3. This is due to the gamma cascade which follows neutron capture by ^{155}Gd and ^{157}Gd [26]. The ^{10}B materials emitted about 0.4 photons per neutron, mainly the 478 keV photon from the $^{10}B(n,\alpha)^7Li$ reaction, while HEB (^{10}B) emitted only 0.13 because its dense heavy element matrix absorbs these photons. For ^{252}Cf neutrons, the photon emission behind 10 cm was 0.74 for Gd loaded reline and 0.63 for Gd-POSS, compared with 0.15 for polyethylene and 0.038 for HEB (^{10}B). The chlorine containing materials also emitted a large number of photons (0.36 for reline, 0.40 for glyceline and 0.44 for $CaCl_2 \cdot 6H_2O$) due to neutron capture by ^{35}Cl, which has a thermal capture cross section of about 44 b [11].

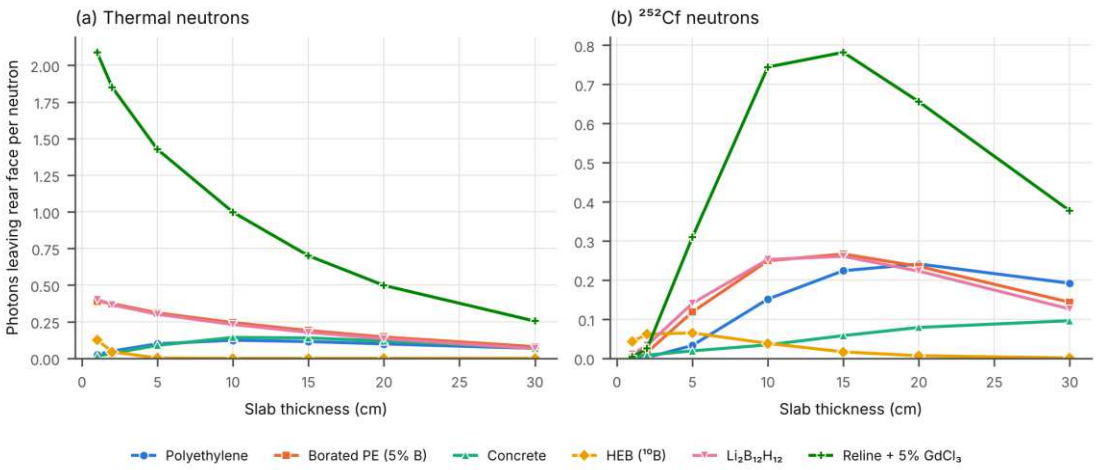


Fig. 10. Photons leaving the rear face per incident neutron against slab thickness for (a) thermal and (b) ^{252}Cf neutrons.

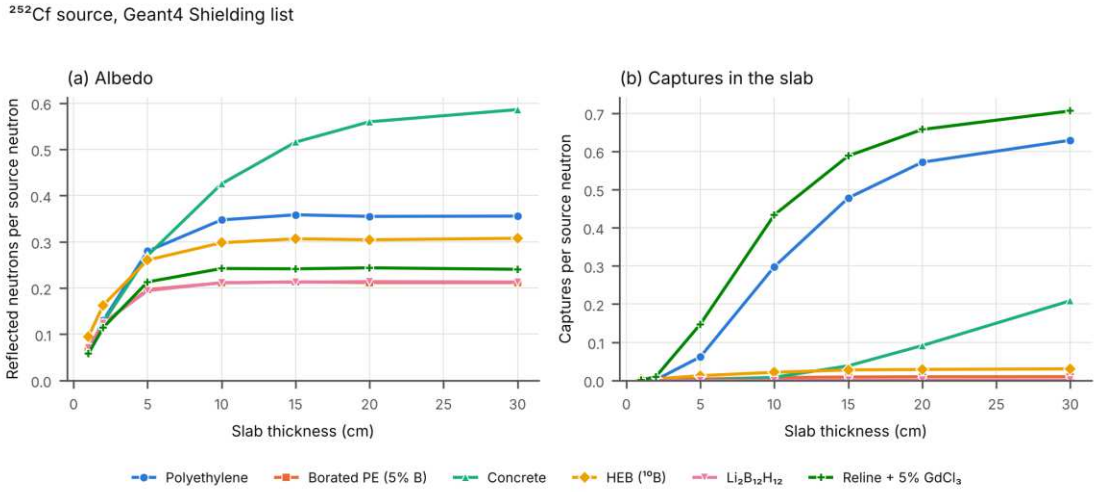


Fig. 11. (a) Neutron albedo and (b) radiative captures in the slab per incident ^{252}Cf neutron against slab thickness.

The albedo and radiative captures for the ^{252}Cf source are shown in Fig. 11. At 30 cm, concrete reflected 0.59 of the incident neutrons, compared with 0.36 for polyethylene and 0.21 for borated polyethylene and $Li_2B_{12}H_{12}$. This is important for room shielding, where reflected neutrons can reach occupied areas. Radiative captures reached 0.71 per neutron in Gd loaded reline and 0.63 in polyethylene but did not exceed 0.03 in the boron compounds. In Geant4, the ^{10}B(n,α) reaction is treated as a charged particle reaction and not as radiative capture. Hence, the boron compounds remove thermal neutrons without producing capture gamma rays, except the 478 keV photon. This explains why boron is preferred over gadolinium when secondary photons must be minimised.

4.3.5. Transmitted neutron spectra

The mean energy of the transmitted neutrons is shown in Fig. 12. The mean energy of the ^{252}Cf spectrum is about 2.1 MeV. Behind polyethylene, the mean energy decreased to 1.4 MeV at 10 cm and 1.8 MeV at 30 cm because thermalised neutrons diffuse out of the slab. Behind 30 cm of borated polyethylene, $Li_2B_{12}H_{12}$ and Gd loaded reline, the mean energy increased to 2.7 to 3.0 MeV because the moderated neutrons were absorbed and only the high energy part of the spectrum was transmitted. Concrete, which has little hydrogen but a large amount of oxygen and silicon, reduced the mean energy to 0.93 MeV. For 14.1 MeV neutrons, the dense materials softened the spectrum the most, with mean energies of 3.5 MeV for Gd_2O_3 and 6.4 MeV for HEB (^{10}B), compared with 7.8 MeV for polyethylene. These changes affect the dose conversion behind the shield and should be considered in the design of layered shields.

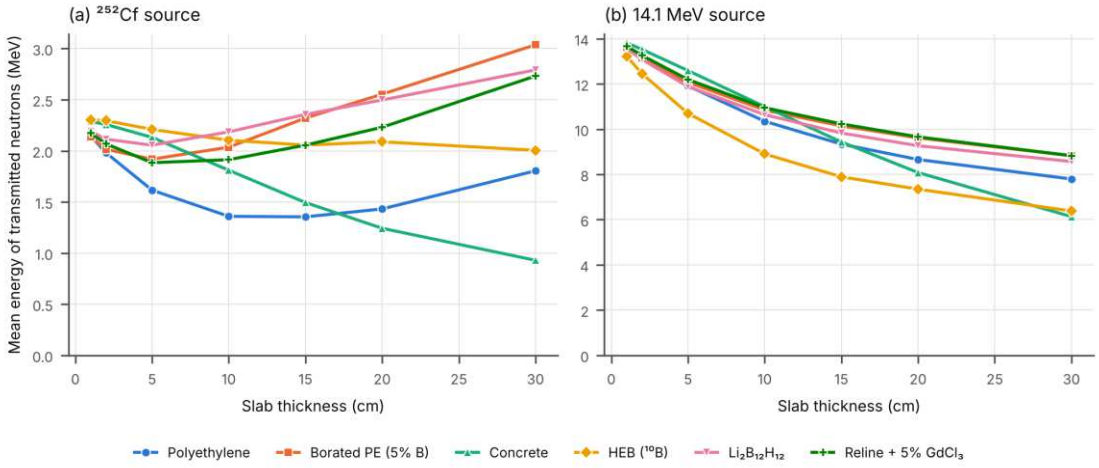


Fig. 12. Mean energy of neutrons leaving the rear face against slab thickness for (a) ^{252}Cf and (b) 14.1 MeV sources.

4.4. High energy charged particles

4.4.1. Dose equivalent

The H/H_0 against areal density for 1 GeV/n iron ions and 1 GeV protons is shown in Fig. 13, and the values behind 20 g/cm² for all materials are shown in Fig. 14 and Table 5. For iron ions, the dose equivalent decreased with areal density for all materials because fragmentation breaks the high LET iron ions into lighter fragments with lower LET. Behind 20 g/cm², LiH gave the lowest value (0.489), followed by $LiBH_4$ (0.571), $Li_2B_{12}H_{12}$ (0.572) and B_4C (0.576). Polyethylene, water and concrete gave 0.631, 0.655 and 0.668, respectively, whereas lead and tungsten both gave 0.903. This trend agrees with accelerator measurements which showed that hydrogen rich and light materials are the most effective per

unit mass against heavy ions [1,5,19]. It was also found that the boron rich closo borate performed similar to $LiBH_4$, which shows that boron contributes to heavy ion shielding as well as neutron shielding.

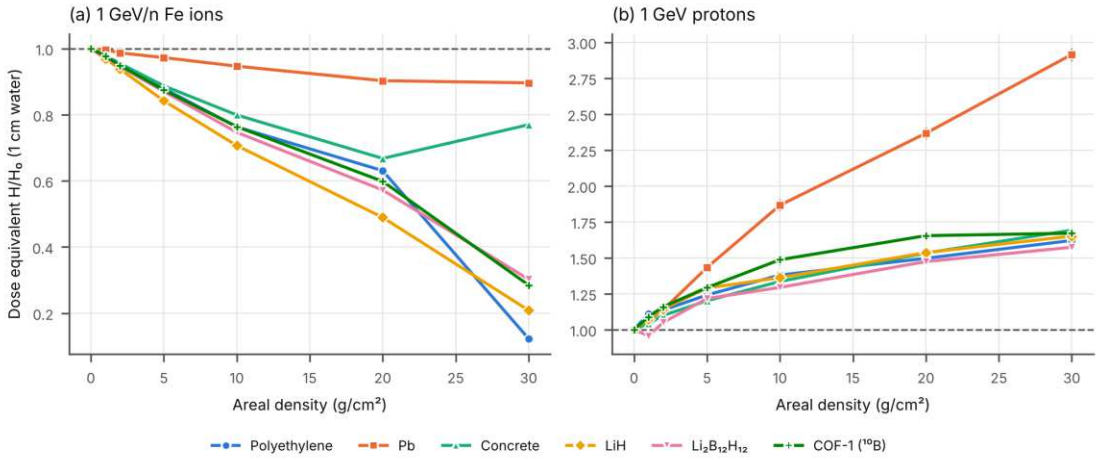


Fig. 13. Dose equivalent ratio H/H_0 in a 1 cm water phantom against shield areal density for (a) 1 GeV/n iron ions and (b) 1 GeV protons.

Table 5. Dose equivalent ratio H/H_0 behind 20 g/cm² of selected materials for four beams.

Material	100 MeV p	1 GeV p	1 GeV/n He	1 GeV/n Fe
LiH	0.007	1.536	1.335	0.489
$LiBH_4$	0.003	1.545	1.376	0.571
$Li_2B_{12}H_{12}$	0.008	1.474	1.378	0.572
B_4C	0.014	1.545	1.467	0.576
Graphane	0.003	1.542	1.342	0.601
Borated PE (5% B)	0.003	1.537	1.294	0.620
LOHC (MCH)	0.001	1.536	1.278	0.629
Polyethylene	0.002	1.496	1.294	0.631
Water	0.003	1.555	1.374	0.655
Concrete	0.008	1.533	1.318	0.668
Aluminum	0.016	1.633	1.344	0.692
HEB (^{10}B)	0.039	2.007	1.477	0.812
Gd_2O_3	0.055	2.109	1.504	0.850
Lead	0.084	2.367	1.463	0.903
Tungsten	0.077	2.415	1.469	0.903

At 30 g/cm², the iron ion curves became non monotonic. The H/H_0 decreased to 0.12 for polyethylene but increased to 0.77 for concrete. The CSDA range of 1 GeV/n iron ions in water is about 27 g/cm². Behind 30 g/cm² of hydrogenous material, the primary ions stopped before the phantom, whereas in concrete, which has a longer range in g/cm², their Bragg peak was inside the phantom. This behaviour is due to the range of the beam and is not a numerical artefact. It should be considered when results for a single beam are generalised to the broad spectrum of galactic cosmic rays [2].

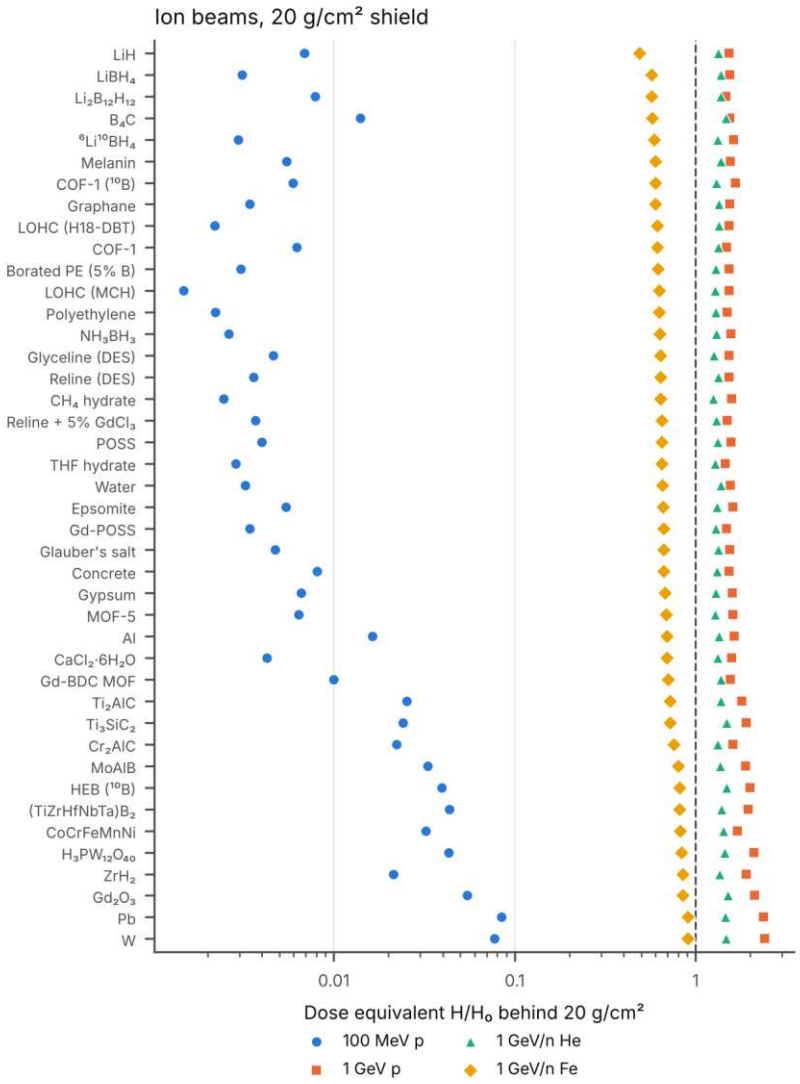


Fig. 14. H/H_0 behind 20 g/cm² for four beams and all materials, sorted by the iron ion result.

For 1 GeV protons and 1 GeV/n helium ions, the dose equivalent increased behind all shields (H/H_0 = 1.26 to 2.42) because the primary particles lose little energy while secondary protons, neutrons and fragments add to the dose. The increase was the lowest for hydrogenous materials (1.46 to 1.62 for protons) and the highest for lead (2.37) and tungsten (2.42). This buildup of secondary particles in high Z materials is the main reason why lead is not used against high energy hadrons. For 100 MeV protons, which stop in about 7.7 g/cm² of water [28], H/H_0 behind 20 g/cm² was 0.001 to 0.008 for the hydrogenous materials and 0.02 to 0.08 for the dense ceramics and metals. In this case, the remaining dose is due to secondary neutrons and photons.

4.4.2. Mean quality factor

The mean quality factor is shown in Fig. 15. For iron ions, $\bar{Q}$ decreased from 22.9 for the unshielded beam to 12.1 behind 30 g/cm² of polyethylene and 13.2 behind LiH, but only to 20.2 behind lead. Therefore, light shields reduce both the dose and its biological effectiveness, which is why the dose equivalent rather than the absorbed dose should be used for comparison [3,27]. For helium ions, $\bar{Q}$ increased slightly with thickness, most strongly in lead (from 1.47 to 1.99), because the target fragments and slowed secondary particles have higher LET.

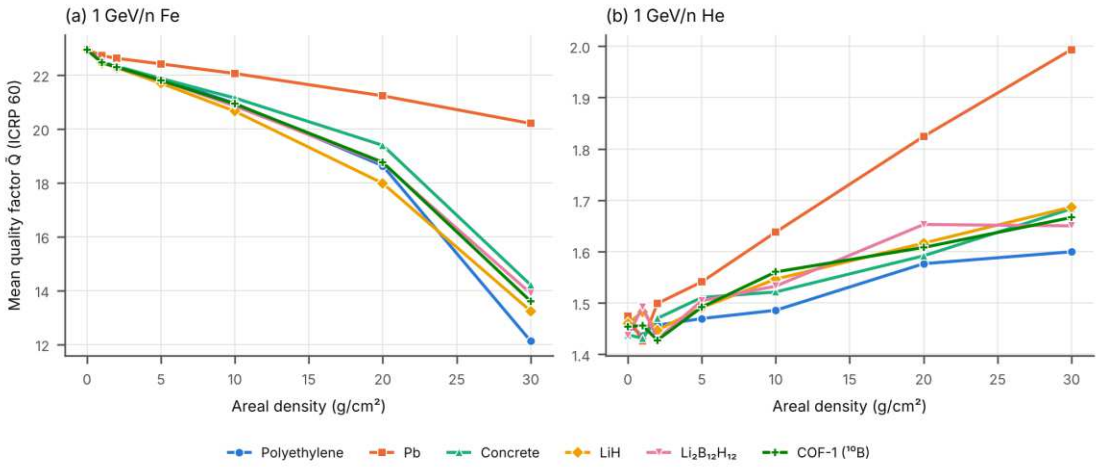


Fig. 15. Mean ICRP 60 quality factor against areal density for (a) 1 GeV/n iron and (b) 1 GeV/n helium ions.

4.4.3. Effect of physics list

The H/H_0 calculated using QBBC and Shielding are compared in Fig. 16. Behind 20 g/cm², QBBC gave on average 12% lower H/H_0 than Shielding for iron ions (ratio 0.69 to 1.02) and 16% higher values for helium ions. For 1 GeV protons, the mean ratio was 0.99. The ranking of materials was the same for both physics lists, but the absolute ion results have a model uncertainty of about 10 to 20%, which is consistent with the known spread of nucleus nucleus interaction models [8,19].

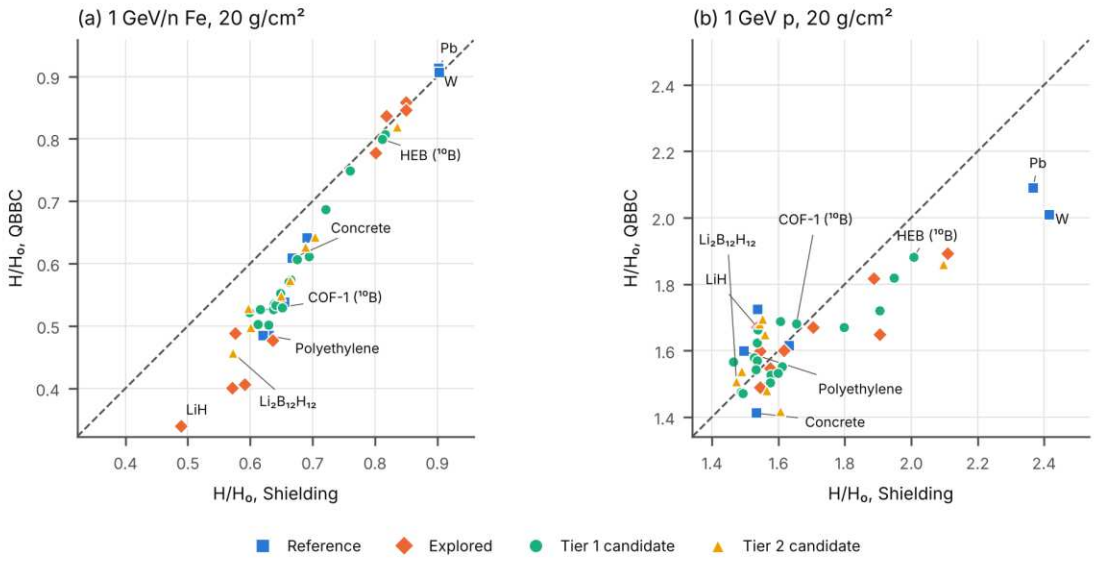


Fig. 16. H/H_0 behind 20 g/cm² calculated using QBBC against Shielding for (a) 1 GeV/n iron ions and (b) 1 GeV protons. The dashed line is the 1:1 line.

4.5. Radiation streaming in TPMS lattices

The ratio of lattice to homogeneous transmission for the four TPMS lattices is shown in Fig. 17 and given in Table 6. For neutrons, all lattices transmitted within 2.3% of the homogeneous slabs because the neutron mean free paths are long compared with the 1 cm cell size. However, for the W and polyethylene gyroid, the uncollided transmission was 12.2 times higher at 662 keV and 2.4 times higher at 1.25 MeV than that of the homogeneous slab. This is because photons streamed through the continuous polyethylene channels, where their mean free path is about 20 times longer than in tungsten. Grading the volume fraction through the thickness reduced the ratio to 5.0 at 662 keV and 1.8 at 1.25 MeV but did not remove it. For the Gd_2O_3 and Glauber's salt and the B_4C and LOHC lattices, whose phases differ less in attenuation, the ratios were 1.01 to 1.04. Therefore, additively manufactured lattices [52] are suitable for neutron shields and low contrast mixed shields. High contrast metal and polymer lattices need cells much smaller than one photon mean free path or an additional homogeneous high Z layer to avoid streaming.

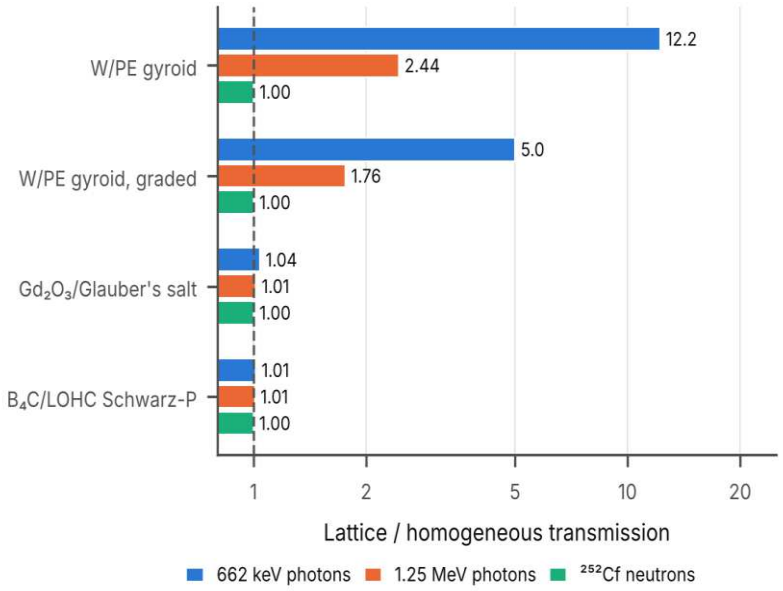


Fig. 17. Ratio of uncollided transmission through a 5 cm TPMS lattice to that through a homogeneous slab of the same composition.

Table 6. Ratio of uncollided transmission through TPMS lattices to that through homogeneous slabs of the same composition.

Lattice	Volume fraction of phase A	662 keV photons	1.25 MeV photons	4.5 MeV neutrons	^{252}Cf neutrons
W/PE gyroid	0.50	12.23	2.44	1.023	1.006
W/PE gyroid, graded	0.50	5.00	1.76	1.017	1.009
Gd_2O_3/Glauber's salt gyroid	0.25	1.04	1.01	1.000	1.002
B_4C/LOHC Schwarz-P	0.48	1.01	1.01	1.001	1.007

4.6. Pearson's correlation analysis

The Pearson's correlation matrix between composition and shielding parameters is given in Table 7. Density was strongly correlated with μ at 662 keV (r = 0.99) and with Z_{eff} (r = 0.91), which confirms that μ at this energy depends mainly on density. Hydrogen content was strongly correlated with Σ_{eff}/ρ (r = 0.97) and moderately correlated with Σ_{eff} (r = 0.61). Gadolinium content was strongly correlated with μ/ρ at 59.5 keV (r = 0.78) due to the K edge of gadolinium. The H/H_0 for iron ions was positively correlated with density (r = 0.83), Z_{eff} (r = 0.81) and μ at 662 keV (r = 0.80) and negatively correlated with hydrogen content (r = −0.65) and Σ_{eff}/ρ (r = −0.73). This shows that the materials which are good per unit mass for neutrons are also good for heavy ions, whereas the materials which are good for photons are poor for heavy ions. The secondary photon emission was weakly correlated with gadolinium content (r = 0.02) because chlorine and boron also produced capture photons in many materials.

Table 7. Pearson's correlation matrix between composition and shielding parameters (n = 42). Z_{eff} is at 662 keV, Σ_{eff} and photons out are for ^{252}Cf neutrons, and H/H₀ Fe is behind 20 g/cm². Values of |r| above 0.30 and 0.39 are significant at $p < 0.05$ and $p < 0.01$, respectively.

	ρ	**H**	**B**	**Gd**	**Z_{eff}**	**μ 662 keV**	**μ/ρ 59.5 keV**	**Σ_{eff}**	**Σ_{eff}/ρ**	**Photons out**	**H/H₀ Fe**
ρ	1										
H	−0.56	1									
B	−0.14	0.23	1								
Gd	0.14	−0.18	−0.10	1							
Z_{eff}	0.91	−0.52	−0.18	0.17	1						
μ 662 keV	0.99	−0.50	−0.13	0.12	0.94	1					
μ/ρ 59.5 keV	0.61	−0.45	−0.17	0.78	0.65	0.60	1				
Σ_{eff}	−0.18	0.61	0.39	−0.10	−0.35	−0.17	−0.16	1			
Σ_{eff}/ρ	−0.59	0.97	0.37	−0.17	−0.56	−0.53	−0.47	0.65	1		
Photons out	−0.34	0.37	0.08	0.02	−0.35	−0.32	−0.18	0.43	0.40	1	
H/H₀ Fe	0.83	−0.65	−0.34	0.26	0.81	0.80	0.73	−0.36	−0.73	−0.28	1

4.7. Comparison with reference shields

The performance of all materials relative to polyethylene on nine parameters is shown in Fig. 18. No material was better than polyethylene for all parameters. The light hydrides and the closo borate were better for neutrons per gram and for iron ions but worse for photons. The dense ceramics and metals were better for photons and D-T neutrons but worse per gram for ^{252}Cf neutrons and heavy ions.

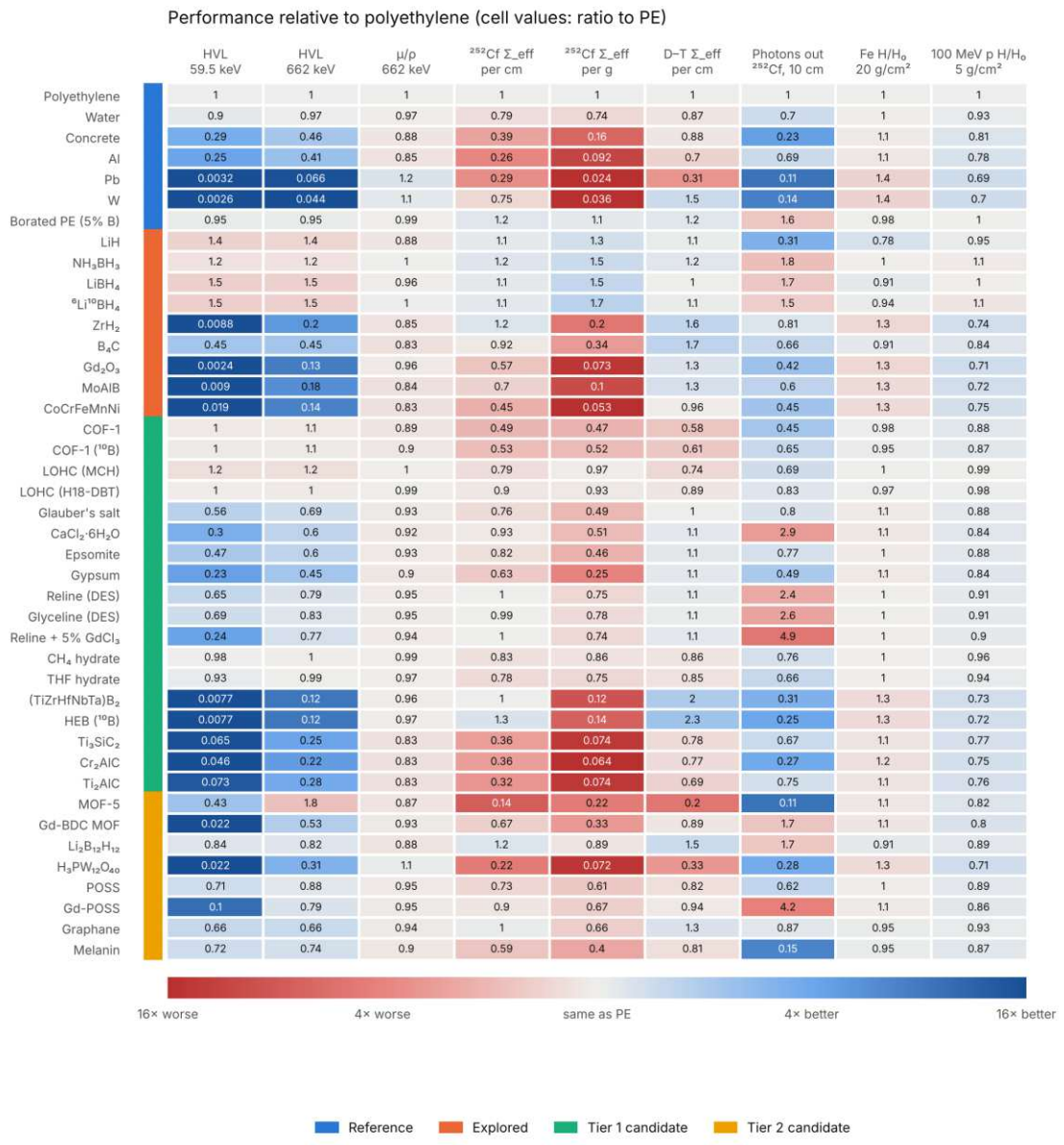


Fig. 18. Performance of 42 materials on nine parameters relative to polyethylene. Cell values are ratios to polyethylene. Blue indicates better and red indicates worse performance.

The HVL at 662 keV is plotted against the ^{252}Cf neutron TVL in Fig. 19. These two parameters are the most relevant for mixed neutron and gamma fields such as reactors and ^{252}Cf source storage. A good mixed field shield lies in the lower left corner of this plot. HEB (^{10}B) was the only material in this region, with an HVL of 0.99 cm and a neutron TVL of 12.7 cm. It was followed by the natural diboride (0.99 and 15.6 cm) and ZrH_2 (1.65 and 13.1 cm). Lead and tungsten were excellent photon shields but poor neutron shields, while the hydrogenous materials, including polyethylene, showed the opposite behaviour. The diboride combines heavy elements for photon attenuation and inelastic scattering, boron for thermal

neutron absorption, and a high density of 8.2 g/cm³. Its low secondary photon emission (Table 4) and the high temperature stability reported for high entropy diborides [32] make it the most promising unexplored material for compact mixed field shields in fusion and reactor applications. However, hydrogen must still be provided by a separate layer or a composite matrix for spectra rich in neutrons below 1 MeV.

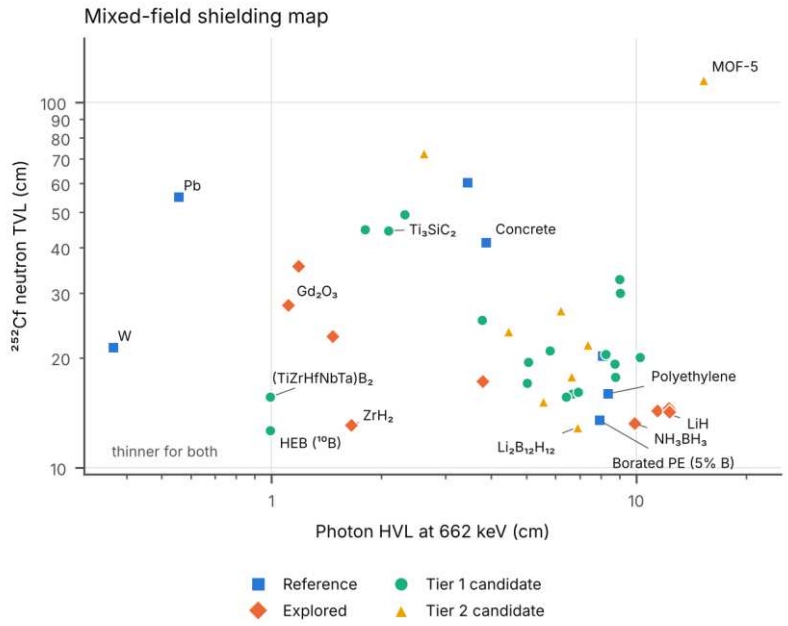


Fig. 19. Mixed field shielding map of photon HVL at 662 keV against ^{252}Cf neutron TVL. Materials in the lower left corner are thin for both types of radiation.

Among the light materials, $Li_2B_{12}H_{12}$ had a neutron TVL of 12.9 cm, the best of all light materials, and the third best iron ion attenuation. It contains about 83 wt% boron and 8 wt% hydrogen and is therefore a promising alternative to borated polyethylene, provided that its thermal and chemical stability in a binder is confirmed [49]. The LOHCs and DES performed close to polyethylene for ^{252}Cf neutrons and iron ions. They are liquids, so they can fill irregular volumes, can be pumped and replaced, and DES can dissolve gadolinium or boron salts [40,42]. Their main drawbacks are lower density and, for chlorine containing solvents, higher secondary photon emission. The salt hydrates and clathrate hydrates behaved like diluted water and offered no shielding advantage, except where their latent heat or ice like structure is useful [43,44]. MOF-5 was the weakest material per unit thickness due to its low density and should be considered only as a host for denser loadings [38,39]. Melanin performed like a low density polymer with no particular advantage apart from its biological origin [51].

4.8. Strengths, limitations, and recommendations

The strengths of this study are the large number of materials, the use of one validated simulation framework for photons, neutrons and heavy ions, the direct calculation of buildup factors and secondary radiation, and the comparison of physics lists.

The limitations of this study are as follows. Many densities were nominal, and several candidates have not been produced in bulk at the assumed density. Results per unit mass do not depend on this assumption, but results per unit thickness do. Thermal scattering data for bound hydrogen were not available for most candidates, which affects the thermal neutron results of hydrogen rich materials by up to about 10% (Section 4.1). Mono energetic ion beams were used instead of a full cosmic ray spectrum, so the ion results describe trends and rankings and not mission doses. The mechanical, thermal and radiation damage properties were taken from the literature and were not modelled.

It is recommended that the high entropy diboride and $Li_2B_{12}H_{12}$ should be synthesised and their attenuation should be measured experimentally using gamma and neutron sources. Layered shields combining the diboride with a hydrogenous liquid should be designed and tested. Thermal scattering data for the hydrogen rich candidates should be generated and included in future simulations. For heavy ions, the most promising materials should be evaluated using a full galactic cosmic ray spectrum.

5. Conclusion

This study concludes that a single Geant4 framework can reliably evaluate photon, neutron and heavy ion shielding for a large set of materials. The simulated photon attenuation coefficients agreed with the calculated values within 0.75% below 15 MeV, and the simulated fast neutron cross sections agreed within 0.5%. The QBBC physics list deviated by up to 99.6% for thermal neutrons in boron and gadolinium compounds and should not be used for neutron shielding. At 662 keV, all materials required between 6.3 and 9.0 g/cm² per HVL, which shows that high Z materials save volume rather than mass. Direct simulation of buildup factors revealed K fluorescence peaks for gadolinium and lead which are not shown by fitted buildup factors. Per unit mass, ^{252}Cf neutron attenuation was governed by hydrogen content ($r = 0.968$), and the empirical removal cross section was a poor predictor ($r = 0.507$). Gadolinium materials captured almost all thermal neutrons but emitted up to 2.1 photons per incident neutron, whereas boron compounds removed neutrons with much fewer secondary photons. Against 1 GeV/n iron ions, LiH, $LiBH_4$, $Li_2B_{12}H_{12}$ and B_4C gave 9 to 23% lower H/H_0 behind 20 g/cm² than polyethylene, while lead and tungsten were the least effective. High contrast W and polyethylene gyroid lattices increased the uncollided 662 keV transmission by a factor of 12 due to streaming, whereas the neutron transmission

through all lattices was within 2.3% of homogeneous slabs. Among the unexplored materials, the ^{10}B enriched $(TiZrHfNbTa)B_2$ high entropy diboride was the best mixed field shield, with an HVL of 0.99 cm at 662 keV, a ^{252}Cf TVL of 12.7 cm, a removal coefficient 2.3 times that of polyethylene at 14.1 MeV and the lowest secondary photon emission among the ten best neutron shields. $Li_2B_{12}H_{12}$ was the best light material for neutrons and heavy ions, and LOHCs and DES are promising pumpable alternatives to polyethylene.

CRediT authorship contribution statement

Mavia Anjum: Writing-review & editing, Writing-original draft, Visualization, Software, Methodology, Investigation, Formal analysis, Data curation, Conceptualization, Data analysis, Simulations. Ansar Abbas: Simulation, Conceptualization, review and editing. Ali Zaman: Methodology, Review and editing. Hannan Younis: Supervision, Validation, Review and editing.

Declaration of Competing Interest

The author declares that there are no conflicts of interest.

Acknowledgments

The authors acknowledge the Research Computing and Data Services of the University of Idaho for providing access to the Lemhi high-performance computing cluster.

Data availability

The Geant4 source code, macros, analysis scripts and result tables are available from the corresponding author on reasonable request.

Supplementary materials

Supplementary Figs. S1 to S7 show the buildup factor against depth at 1 MeV, ^{252}Cf transmission curves, the relation between neutron attenuation and secondary photons, the composition of transmitted neutron spectra, proton ranges and stopping powers compared with PSTAR, neutron cross sections against energy, and electron and alpha particle ranges.

Ethical Statement

No human or animal subjects were used during this study.

Funding Statement

This work did not receive any funding.

Ethics, Consent to Participate, and Consent to Publish declarations

Not applicable

References

[1] S. Guetersloh, C. Zeitlin, L. Heilbronn, J. Miller, T. Komiyama, A. Fukumura, Y. Iwata, T. Murakami, M. Bhattacharya, Polyethylene as a radiation shielding standard in simulated cosmic-ray environments, Nuclear Instruments and Methods in Physics Research Section B 252 (2006) 319–332. https://doi.org/10.1016/j.nimb.2006.08.019.

[2] T.C. Slaba, A.A. Bahadori, B.D. Reddell, R.C. Singleterry, M.S. Clowdsley, J.W. Norbury, Optimal shielding thickness for galactic cosmic ray environments, Life Sciences in Space Research 12 (2017) 1–15. https://doi.org/10.1016/j.lssr.2016.12.003.

[3] International Commission on Radiological Protection, The 2007 Recommendations of the International Commission on Radiological Protection. ICRP Publication 103, Elsevier, Oxford, 2007.

[4] S.A. Thibeault, J.H. Kang, G. Sauti, C. Park, C.C. Fay, G.C. King, Nanomaterials for radiation shielding, MRS Bulletin 40 (2015) 836–841. https://doi.org/10.1557/mrs.2015.225.

[5] M. Naito, S. Kodaira, R. Ogawara, K. Tobita, Y. Someya, T. Kusumoto, et al., Investigation of shielding material properties for effective space radiation protection, Life Sciences in Space Research 26 (2020) 69–76. https://doi.org/10.1016/j.lssr.2020.05.001.

[6] S. Agostinelli, J. Allison, K. Amako, J. Apostolakis, H. Araujo, P. Arce, M. Asai, et al., Geant4 - a simulation toolkit, Nuclear Instruments and Methods in Physics Research Section A 506 (2003) 250–303. https://doi.org/10.1016/S0168-9002(03)01368-8.

[7] J. Allison, K. Amako, J. Apostolakis, H. Araujo, P. Arce Dubois, M. Asai, G. Barrand, et al., Geant4 developments and applications, IEEE Transactions on Nuclear Science 53 (2006) 270–278. https://doi.org/10.1109/TNS.2006.869826.

[8] J. Allison, K. Amako, J. Apostolakis, P. Arce, M. Asai, T. Aso, E. Bagli, et al., Recent developments in Geant4, Nuclear Instruments and Methods in Physics Research Section A 835 (2016) 186–225. https://doi.org/10.1016/j.nima.2016.06.125.

[9] P. Arce, D. Bolst, M.-C. Bordage, J.M.C. Brown, P. Cirrone, M.A. Cortés-Giraldo, D. Cutajar, et al., Report on G4-Med, a Geant4 benchmarking system for medical physics applications developed by the Geant4 Medical Simulation Benchmarking Group, Medical Physics 48 (2021) 19–56. https://doi.org/10.1002/mp.14226.

[10] L. Thulliez, C. Jouanne, E. Dumonteil, Improvement of Geant4 Neutron-HP package: From methodology to evaluated nuclear data library, Nuclear Instruments and Methods in Physics Research Section A 1027 (2022) 166187. https://doi.org/10.1016/j.nima.2021.166187.

[11] D.A. Brown, M.B. Chadwick, R. Capote, A.C. Kahler, A. Trkov, M.W. Herman, A.A. Sonzogni, et al., ENDF/B-VIII.0: The 8th major release of the nuclear reaction data library with CIELO-project cross sections, new standards and thermal scattering data, Nuclear Data Sheets 148 (2018) 1–142. https://doi.org/10.1016/j.nds.2018.02.001.

[12] M.J. Berger, J.H. Hubbell, S.M. Seltzer, J. Chang, J.S. Coursey, R. Sukumar, D.S. Zucker, K. Olsen, XCOM: Photon Cross Sections Database (NIST Standard Reference Database 8), (2010). https://physics.nist.gov/PhysRefData/Xcom/Text/XCOM.html (accessed October 13, 2026).

[13] E. Şakar, Ö.F. Özpolat, B. Alım, M.I. Sayyed, M. Kurudirek, Phy-X / PSD: Development of a user friendly online software for calculation of parameters relevant to radiation shielding and dosimetry, Radiation Physics and Chemistry 166 (2020) 108496. https://doi.org/10.1016/j.radphyschem.2019.108496.

[14] B. Aygün, E. Şakar, T. Korkut, M.I. Sayyed, A. Karabulut, M.H.M. Zaid, Fabrication of Ni, Cr, W reinforced new high alloyed stainless steels for radiation shielding applications, Results in Physics 12 (2019). https://doi.org/10.1016/j.rinp.2018.11.038.

[15] B. Aygün, E. Şakar, V.P. Singh, M.I. Sayyed, T. Korkut, A. Karabulut, Experimental and Monte Carlo simulation study on potential new composite materials to moderate neutron-gamma radiation, Progress in Nuclear Energy 130 (2020) 103538. https://doi.org/10.1016/j.pnucene.2020.103538.

[16] H. Tunç, T. Tuğrul, B. Oto, H.E. Yildiz, Effect of Re/Nb ratio on gamma-ray attenuation in high-entropy alloys: A combined Geant4 simulation and EpiXS analysis, Nuclear Instruments and Methods in Physics Research Section B 577 (2026).

[17] M.A. Al Zaman, L.A. Kunja, Effectiveness of radiation shields constructed from Martian regolith and different polymers for human habitat on Mars using MULASSIS/GEANT4 and OLTARIS, AIP Advances 13 (2023). https://doi.org/10.1063/5.0163306.

[18] L.A. Kunja, Y. Yi, E. Kim, J. Sohn, J. Jung, Performance of hydrogen-rich materials in combination with lunar regolith for shielding against GCR, albedo, and SPEs on the surface of the moon studied using MULASSIS, AIP Advances 15 (2025). https://doi.org/10.1063/5.0293969.

[19] F. Luoni, D. Boscolo, G. Fiore, L. Bocchini, F. Horst, C.-A. Reidel, C. Schuy, C. Cipriani, et al., Dose attenuation in innovative shielding materials for radiation protection in space: Measurements and simulations, Radiation Research 198 (2022). https://doi.org/10.1667/RADE-22-00147.1.

[20] Geant4 Collaboration, Guide for Physics Lists, Geant4 Documentation (n.d.). https://geant4.web.cern.ch/documentation/dev/plg_html/PhysicsListGuide/physicslistguide.html (accessed October 13, 2026).

[21] J.H. Hubbell, S.M. Seltzer, Tables of X-ray mass attenuation coefficients and mass energy-absorption coefficients 1 keV to 20 MeV for elements Z = 1 to 92 and 48 additional substances of dosimetric interest, National Institute of Standards and Technology, Gaithersburg, MD, 1995. https://nvlpubs.nist.gov/nistpubs/Legacy/IR/nistir5632.pdf.

[22] H. Yilmaz Alan, O. Guler, A. Yilmaz, L.A. Susam, E. Kavaz, G. Kılıç, et al., Exploring nuclear radiation shielding capabilities of high-entropy carbides: A study on composition and effectiveness, Nuclear Technology 212 (2026) 1249–1272.

[23] Y. Harima, An approximation of gamma-ray buildup factors by modified geometrical progression, Nuclear Science and Engineering 83 (1983) 299–309. https://doi.org/10.13182/NSE83-A18222.

[24] Z. Li, Y. Han, A. Wang, D. Zhao, L. Fan, L. He, S. Zhang, P. Cheng, H. Liu, Z. Chai, S. Wang, Efficient neutron radiation shielding by boron-lithium imidazolate frameworks, Dalton Transactions 51 (2022) 11625–11629. https://doi.org/10.1039/D2DT01825J.

[25] C. Hu, Y.-T. Zhai, L.-L. Song, X.-D. Mao, Structure-thermal activity relationship in a novel polymer/MOF-based neutron-shielding material, Polymer Composites (2019). https://doi.org/10.1002/pc.25465.

[26] J. Chen, X. Zhang, W. Xiao, D. Pan, W. Wu, Advances in gadolinium-based composite materials for neutron and gamma-ray shielding, Frontiers in Materials 12 (2025) 1561198. https://doi.org/10.3389/fmats.2025.1561198.

[27] International Commission on Radiological Protection, 1990 Recommendations of the International Commission on Radiological Protection. ICRP Publication 60, Pergamon Press, Oxford, 1991.

[28] M.J. Berger, J.S. Coursey, M.A. Zucker, J. Chang, ESTAR, PSTAR, and ASTAR: Computer programs for calculating stopping-power and range tables for electrons, protons, and helium ions (NIST Standard Reference Database 124), (2005). https://physics.nist.gov/Star (accessed October 13, 2026).

[29] J.F. Ziegler, M.D. Ziegler, J.P. Biersack, SRIM – The stopping and range of ions in matter (2010), Nuclear Instruments and Methods in Physics Research Section B 268 (2010) 1818–1823. https://doi.org/10.1016/j.nimb.2010.02.091.

[30] J.-W. Yeh, S.-K. Chen, S.-J. Lin, J.-Y. Gan, T.-S. Chin, T.-T. Shun, C.-H. Tsau, S.-Y. Chang, Nanostructured high-entropy alloys with multiple principal elements: Novel alloy design concepts and outcomes, Advanced Engineering Materials 6 (2004) 299–303. https://doi.org/10.1002/adem.200300567.

[31] B. Cantor, I.T.H. Chang, P. Knight, A.J.B. Vincent, Microstructural development in equiatomic multicomponent alloys, Materials Science and Engineering: A 375-377 (2004) 213–218. https://doi.org/10.1016/j.msea.2003.10.257.

[32] J. Gild, Y. Zhang, T. Harrington, S. Jiang, T. Hu, M.C. Quinn, W.M. Mellor, N. Zhou, K. Vecchio, J. Luo, High-entropy metal diborides: A new class of high-entropy materials and a new type of ultrahigh temperature ceramics, Scientific Reports 6 (2016) 37946. https://doi.org/10.1038/srep37946.

[33] M.W. Barsoum, The MN+1AXN phases: A new class of solids; thermodynamically stable nanolaminates, Progress in Solid State Chemistry 28 (2000) 201–281. https://doi.org/10.1016/S0079-6786(00)00006-6.

[34] M.A. Tunes, S.M. Drewry, J.D. Arregui-Mena, S. Picak, G. Greaves, L.B. Cattini, S. Pogatscher, et al., Accelerated radiation tolerance testing of Ti-based MAX phases, Materials Today Energy 30 (2022) 101186.

[35] S. Kota, M. Sokol, M.W. Barsoum, A progress report on the MAB phases: Atomically laminated, ternary transition metal borides, International Materials Reviews 65 (2020) 226–255. https://doi.org/10.1080/09506608.2019.1637090.

[36] H. Zhang, J.Y. Kim, R. Su, P. Richardson, J. Xi, E. Kisi, J. O'Connor, L. Shi, I. Szlufarska, Defect behavior and radiation tolerance of MAB phases (MoAlB and Fe2AlB2) with comparison to MAX phases, Acta Materialia 196 (2020) 505–515. https://doi.org/10.1016/j.actamat.2020.07.002.

[37] A.P. Côté, A.I. Benin, N.W. Ockwig, M. O'Keeffe, A.J. Matzger, O.M. Yaghi, Porous, crystalline, covalent organic frameworks, Science 310 (2005) 1166–1170. https://doi.org/10.1126/science.1120411.

[38] H. Li, M. Eddaoudi, M. O'Keeffe, O.M. Yaghi, Design and synthesis of an exceptionally stable and highly porous metal-organic framework, Nature 402 (1999) 276–279. https://doi.org/10.1038/46248.

[39] S.E. Gilson, M. Fairley, P. Julien, A.G. Oliver, S.L. Hanna, G. Arntz, O.K. Farha, J.A. LaVerne, P.C. Burns, Unprecedented radiation resistant thorium–binaphthol metal–organic framework, Journal of the American Chemical Society 142 (2020) 13299–13304.

[40] P. Preuster, C. Papp, P. Wasserscheid, Liquid organic hydrogen carriers (LOHCs): Toward a hydrogen-free hydrogen economy, Accounts of Chemical Research 50 (2017) 74–85. https://doi.org/10.1021/acs.accounts.6b00474.

[41] A.P. Abbott, G. Capper, D.L. Davies, R.K. Rasheed, V. Tambyrajah, Novel solvent properties of choline chloride/urea mixtures, Chemical Communications (2003) 70–71. https://doi.org/10.1039/b210714g.

[42] E.L. Smith, A.P. Abbott, K.S. Ryder, Deep eutectic solvents (DESs) and their applications, Chemical Reviews 114 (2014) 11060–11082. https://doi.org/10.1021/cr300162p.

[43] B. Zalba, J.M. Marín, L.F. Cabeza, H. Mehling, Review on thermal energy storage with phase change: Materials, heat transfer analysis and applications, Applied Thermal Engineering 23 (2003) 251–283. https://doi.org/10.1016/S1359-4311(02)00192-8.

[44] E.D. Sloan, Fundamental principles and applications of natural gas hydrates, Nature 426 (2003) 353–359. https://doi.org/10.1038/nature02135.

[45] J.O. Sofo, A.S. Chaudhari, G.D. Barber, Graphane: A two-dimensional hydrocarbon, Physical Review B 75 (2007) 153401. https://doi.org/10.1103/PhysRevB.75.153401.

[46] D.C. Elias, R.R. Nair, T.M.G. Mohiuddin, S.V. Morozov, P. Blake, M.P. Halsall, A.C. Ferrari, D.W. Boukhvalov, M.I. Katsnelson, A.K. Geim, K.S. Novoselov, Control of graphene's properties by reversible hydrogenation: Evidence for graphane, Science 323 (2009) 610–613. https://doi.org/10.1126/science.1167130.

[47] F.H. Stephens, V. Pons, R.T. Baker, Ammonia–borane: the hydrogen source par excellence?, Dalton Transactions (2007) 2613–2626. https://doi.org/10.1039/b703053c.

[48] A. Züttel, P. Wenger, S. Rentsch, P. Sudan, P. Mauron, C. Emmenegger, LiBH4 a new hydrogen storage material, Journal of Power Sources 118 (2003) 1–7. https://doi.org/10.1016/S0378-7753(03)00054-5.

[49] J.-H. Her, M. Yousufuddin, W. Zhou, S.S. Jalisatgi, J.G. Kulleck, J.A. Zan, S.-J. Hwang, R.C. Bowman, T.J. Udovic, Crystal structure of Li2B12H12: A possible intermediate species in the decomposition of LiBH4, Inorganic Chemistry 47 (2008) 9757–9759. https://doi.org/10.1021/ic801345h.

[50] D.-L. Long, E. Burkholder, L. Cronin, Polyoxometalate clusters, nanostructures and materials: From self assembly to designer materials and devices, Chemical Society Reviews 36 (2007) 105–121. https://doi.org/10.1039/B502666K.

[51] E. Dadachova, R.A. Bryan, X. Huang, T. Moadel, A.D. Schweitzer, P. Aisen, J.D. Nosanchuk, A. Casadevall, Ionizing radiation changes the electronic properties of melanin and enhances the growth of melanized fungi, PLoS ONE 2 (2007) e457. https://doi.org/10.1371/journal.pone.0000457.

[52] O. Al-Ketan, R.K. Abu Al-Rub, Multifunctional mechanical metamaterials based on triply periodic minimal surface lattices, Advanced Engineering Materials 21 (2019) 1900524. https://doi.org/10.1002/adem.201900524.

[53] International Organization for Standardization, Neutron reference radiations fields. Part 1: Characteristics and methods of production, (2021).

Supplementary Files

This is a list of supplementary files associated with this preprint. Click to download.

- SupplementaryData.docx